Basin-scale stratigraphic correlation of late Pleistocene-Holocene (MIS 5e-MIS 1) strata across the rapidly subsiding Po Basin (northern Italy)

Published Version:
Basin-scale stratigraphic correlation of late Pleistocene-Holocene (MIS 5e-MIS 1) strata across the rapidly subsiding Po Basin (northern Italy) / Campo B.; Bruno L.; Amorosi A.. - In: QUATERNARY SCIENCE REVIEWS. - ISSN 0277-3791. - ELETTRONICO. - 237:(2020), pp. 106300.1-106300.22. [10.1016/j.quascirev.2020.106300]

Availability:
This version is available at: https://hdl.handle.net/11585/806554 since: 2021-02-25

Published:
DOI: http://doi.org/10.1016/j.quascirev.2020.106300

Basin-scale stratigraphic correlation of Late Pleistocene-Holocene (MIS 5e-MIS 1) strata across the rapidly subsiding Po Basin (northern Italy)

Campo B.[1*], Bruno L.[2], Amorosi A.[1]

[1] Dipartimento di Scienze Biologiche, Geologiche ed Ambientali (BiGeA), Università degli Studi di Bologna, Piazza di Porta San Donato 1, 40126, Bologna (Italy). E-mail addresses: bruno.campo@unibo.it (* corresponding author); alessandro.amorosi@unibo.it.

[2] Dipartimento di Scienze Chimiche e Geologiche, Università degli Studi di Modena e Reggio Emilia, Via Giuseppe Campi 103, 41125, Modena (Italy). E-mail address: luigi.bruno@unimore.it.

Highlights

- The stratigraphic architecture of the last 130 ky in the Po Basin was reconstructed
- Along-strike and along-dip facies changes are emphasized through transects
- Detailed facies mapping of the MIS 5e maximum marine ingression has been provided
- MIS 5e-MIS 1 facies architecture clearly denotes a main glacio-eustatic control
- Detailed stratigraphic correlations reveal a structural control on sedimentation

Abstract

Eight stratigraphic transects, 40 to 140 km long reveal, for the first time on a regional scale, a comprehensive picture of facies architecture of the highly preserved Late Pleistocene-Holocene sedimentary succession from the rapidly subsiding Po Basin. Facies analysis and pollen-based correlation, supported by radiocarbon, electron-spin resonance and optically stimulated luminescence dates, enabled the attribution of distinct stratigraphic intervals to Marine Isotope Stages (MIS) 6 to 1.

Basin-scale facies changes appear to have been driven mostly by glacio-eustatic oscillations falling in the Milankovitch band (~100 ky). The MIS 5e coastal wedge was tracked continuously beneath the modern shoreline, for over 110 km along strike. Along-dip (west-east) stratigraphic correlation over 140 km revealed

the characteristic landward transition from shallow-marine and coastal facies to lagoonal, swamp, and floodplain deposits.

The MIS 5d-MIS 2 stratigraphic succession, up to 95-m-thick, records the stepped, basinward shift of facies related to the post-MIS 5e sea-level fall. In particular, lagoon and swamp facies mark minor transgressions (Substages 5c and 5a), whereas thick floodplain deposits and laterally extensive (> 40 km) fluvial channel-belts, up to 30 m thick, characterized the glacial periods (MIS 4 and MIS 2).

The Holocene (MIS 1) coastal wedge shares many similarities in terms of facies architecture and geometry with its MIS 5e counterpart, though maximum landward marine incursion during the MIS 5e transgression was 10 km farther inland (35 km inland of modern shoreline). Organic-rich (freshwater swamp) environments developed > 100 km landwards of the present-day coastline.

The MIS 5e-MIS 1 succession of the Po Basin displays an exceptional thickness, up to 130 m. Minimum values (~20 m) are recorded close to the Apennine margin and above the buried actively growing anticlines. The spatial distribution and geometry of the MIS 5e-MIS 1 strata, as well as rapidly varying subsidence rates (from 0.2 to 1.0 mm/y) reflect the strong influence of the structural setting (location of major thrust fronts) over the creation/destruction of accommodation.

Keywords: Late Quaternary; Last Interglacial; MIS 5e coastal wedge; Maximum marine ingression; Po Basin.

1. Introduction

The Last Interglacial (LI) coincides with Marine Isotope Stage (MIS) 5e, which is a proxy record of low global ice volume and high sea-level (Kukla et al., 2002). MIS 5e is the lowest substage of MIS 5 (Shackleton, 1969), which spans the time interval between Termination II (end of MIS 6,~135 ky BP) and the onset of MIS 5d (~116 ky BP; Murray-Wallace, 2013; Shackleton et al., 2003).

The MIS 5e interval was characterized by warmer climate conditions and higher global sea-level (up to 9 m) than the present interglacial (MIS 1; Antonioli, 2012; Dutton et al., 2015; Dutton and Lambeck, 2012; Kopp et al., 2009; Tzedakis et al., 2018; Waelbroeck et al., 2002). For this reason, the LI is generally considered a good analog, albeit imperfect, of possible scenarios resulting from the ongoing global warming (Antonioli et al., 2017; Clark and Huybers, 2009; IPCC, 2018, 2007; Overpeck et al., 2006; Sánchez Goñi et al., 2012, 1999; Tzedakis, 2013) and its near-future projections (Church et al., 2013; Horton et al., 2019; Rohling et al., 2008; Stammer et al., 2019).

Climate and relative sea-level characteristics of MIS 5e have been typically reconstructed from ice and marine cores (Bard et al., 1990; Chappell and Shackleton, 1986; Chappell et al., 1996; Shackleton, 2000, 1987; Siddall et al., 2003; Waelbroeck et al., 2002). On the other hand, LI sea-level has been estimated through the analysis of geomorphological and stratigraphical features, such as prominent tidal notches, lagoonal sedimentary facies, fossil beaches and marine terraces (Lambeck et al., 2004; Murray-Wallace, 2013; Pirazzoli, 1993; Rovere et al., 2016) or submerged speleothems (Antonioli et al., 2004; Bard et al., 2002). These sea-level indicators have also been used as a regional datum to quantify geodetic variations over the last 120 ky (Bordoni and Valensise, 1998; Murray-Wallace, 2002). In general, MIS 5e deposits are worldwide considered as important stratigraphic markers (Creveling et al., 2015; Murray-Wallace and Woodroffe, 2014) and have been used to assess vertical displacements due to regional subsidence or uplift (Ferranti et al., 2010, 2006; Galili et al., 2007; Guillaume et al., 2013; Lambeck et al., 2004; Matsu'ura et al., 2019; Rovere et al., 2016). MIS 5e sea-level markers have been documented worldwide in sub-aerially exposed successions in stable or uplifting areas (Amorosi et al., 2014; Bardají et al., 2009; Carr et al., 2010; Mauz et al., 2012; Murray-Wallace et al., 2016; Oliver et al., 2018), or buried beneath subsiding coastal plains (Carboni et al., 2010; De Santis et al., 2010; Otvos, 2015, 2013).

In spite of the huge number of studies that focused on the LI sedimentary record, scarce attention has been paid, in general, to detailed stratigraphic reconstructions of facies architecture, nor accurate sedimentological studies have been undertaken on buried late Pleistocene successions. In relatively proximal (alluvial) settings, the post-MIS 5e stratigraphy is generally poorly preserved due to river incision driven by sea-level fall (Blum et al., 2013; Milli et al., 2016, 2013; Otvos, 2005; Tropeano et al., 2013; Vis et al., 2008). By contrast, detailed stratigraphic information is available for the Rhine-Meuse system (the Netherlands), a low-gradient fluvial system developed in a slowly subsiding setting (Busschers et al., 2005, 2007; Peeters et al., 2019, 2015; Sier et al., 2015). However, because of river avulsion and erosion during the last 130 ky, the MIS 5-MIS 2 stratigraphic record (up to 40 m thick), has only locally been preserved (Peeters et al., 2016, 2015). Additional high-resolution studies carried out in the Kanto and Echigo coastal plains, in Japan, have been limited to the MIS 5e or MISs 3-1 intervals (Nakazawa et al., 2017; Tanabe et al., 2013, 2009).

In the Po Basin (Northern Italy, Fig. 1), high subsidence rates (up to 2.5 mm/y over the last 1.43 My; Carminati and Di Donato, 1999) have led to the deposition of a stratigraphically extensive late Quaternary succession (Regione Emilia-Romagna and Eni-Agip, 1998; Regione Lombardia and Eni Divisione Agip, 2002). Several studies, focusing on relatively small areas or even on single cores (Amorosi et al., 2004, 1999a; Castorina and Vaiani, 2018; Fiorini, 2004; Scarponi and Kowalewski, 2004), have documented an almost continuous and highly-resolved sedimentary record of the last 140 ky. These studies documented the presence of a thick coastal sediment wedge at depths of up to 100 m. Local studies from the central Po Plain, up to 140 km landwards of the modern shoreline, showed clear changes in pollen taxa and lithofacies within a fully alluvial succession (Amorosi et al., 2008, 2001; Geological Map of Italy at 1:50,000 scale, Sheets: 187, 200, 223, 240, 255), which are interpreted to represent the abrupt change from cold (MIS 6, 4, 3 and 2) to temperate (MIS 5e and 1) climatic conditions.

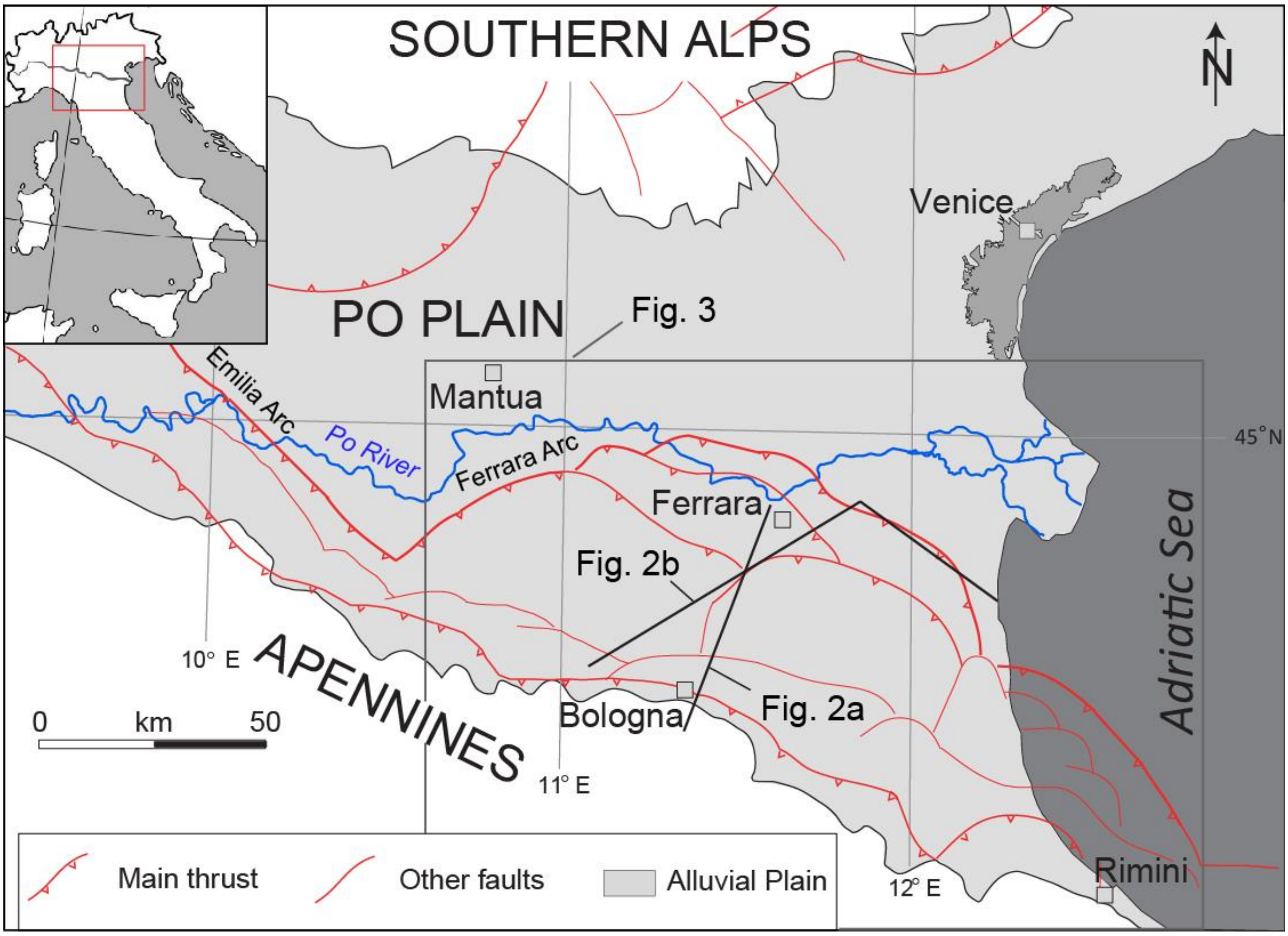

Fig. 1 – Structural map of the Po Plain, indicating the (i) buried Alpine and Apennine structures (modified from Burrato et al., 2003); (ii) study area (gray rectangle), and (iii) traces of seismic and stratigraphic profiles of Figure 2a, b.

Despite all these data, no stratigraphic reconstruction is currently available for the MIS 5e and post-MIS 5e sedimentary record at basin-scale. Whereas MIS 3-MIS 1 stratigraphy, and particularly the depositional architecture of the Holocene coastal wedge, have been studied in detail (Amorosi et al., 2019, 2017a; Bruno et al., 2017; Campo et al., in press, 2017), older Late Pleistocene strata are poorly known, especially in terms of lateral facies distribution and geometry of sedimentary bodies.

This work presents, for the first time, a high-resolution reconstruction of the stratigraphic architecture of the Po Basin succession of the last 130 ky. This study focusses on: (i) the basin-scale correlation of the MIS 5e coastal wedge and the identification of its landward equivalents; (ii) the reconstruction of its 3D geometries, with a specific focus on along-dip and along-strikes facies variations; (iii) the mapping of the maximum marine ingression during the MIS 5e highstand; (iv) the critical analysis of controlling-factors of facies distribution and thickness of MIS 5e deposits.

2. Geological setting

2.1 Structural setting

The Po Plain is the widest alluvial plain (~ 48,000 km^2) of the Italian peninsula. It is the morphological expression of the Po Basin, a rapidly subsiding basin bounded by the south-verging Southern Alps and the north-verging Northern Apennines (Burrato et al., 2003; Fig. 1). These two orogens started to form in the Cretaceous, in response to the collision of the Adria microplate and the European Plate (Carminati and Doglioni, 2012). The Northern Apennines are a fold-and-thrust belt that formed mostly during the Neogene and the Quaternary (Basili and Barba, 2007; Malinverno and Ryan, 1986; Royden et al., 1987). The most external thrusts of the Apennines are buried beneath the Miocene to Quaternary sedimentary infill of the southern Po Basin (Pieri and Groppi, 1981; Figs. 1, 2a). In the central and eastern sectors of the Po Plain, the buried structures of the Northern Apennines consist of two arched thrust systems, with convexity towards the NNE (Fig. 1): the Emilia arc to the W and the Ferrara arc to the SE (Fig. 1). These thrust systems became active in the Late Miocene (Boccaletti et al., 2011; Picotti and Pazzaglia, 2008; Scrocca et al., 2007) and, following the 2012 seismic events in the southern Po Plain (i.e. Emilia Earthquake, 2012; Caputo et al., 2015; Pondrelli et al., 2012) they are considered to be still active. Fault propagation and imbrication led to the formation of thrust-related anticlines (Maesano et al., 2015; Ori and Friend, 1984; Rossi et al., 2015; Toscani et al., 2014). Far away from anticline culminations, subsidence rates have been estimated to be as high as 2.5 mm/y over the last 1.43 My (Carminati et al., 2003; Carminati and Di Donato, 1999).

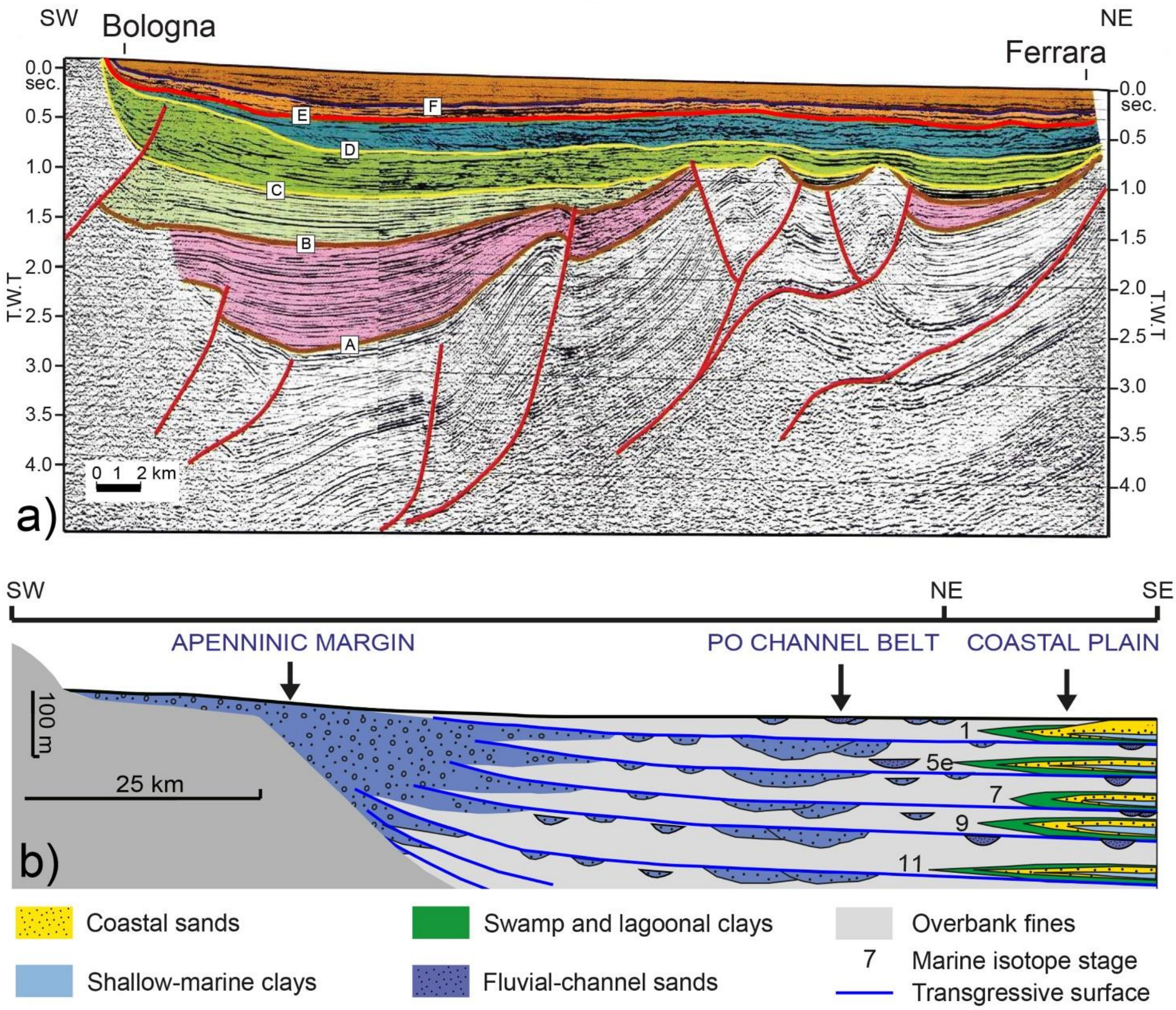

Fig. 2 – a) Interpreted seismic profile showing the Plio-Quaternary sedimentary infill of the Po Basin (colored area): depositional sequences (P2, Qm and Qc), major blind thrusts (red lines) and stratigraphic unconformities (A-F lines) are shown as interpreted by Regione Emilia-Romagna and ENI-Agip, (1998; location in Figure 1). T.W.T. – two-way travel time. For a depth-version of the same seismic profile, see Boccaletti et al. (2011), their Fig. 5, cross-section D-D’. b) Schematic illustration of the proximal-to-distal

stratigraphic architecture of the Middle-Late Pleistocene Po Plain succession, showing distinct cyclic changes in facies and channel stacking in the Milankovitch band (~ 100 ky). Modified from Amorosi and Colalongo (2005). Location can be found in Figure 1.

2.2 Stratigraphic setting

The sedimentary infill of the Po Basin has been investigated at basin-scale through the integration of seismic and well data (Amadori et al., 2019; Ghielmi et al., 2013; Pieri and Groppi, 1981; Regione Emilia-Romagna and Eni-Agip, 1998; Regione Lombardia and Eni Divisione Agip, 2002). The Plio-Quaternary succession ranges in thickness between 8 km in the depocenters, to a few hundred meters atop the buried anticlines (Mariotti and Doglioni, 2000; Pieri and Groppi, 1981). It is characterized by a shallowing-upward trend, from Pliocene deep-marine to Quaternary shallow-marine and continental deposits (Ori, 1993; Ricci Lucchi et al., 1982). Based on magnetostratigraphic data (Muttoni et al., 2003), the uppermost ~800 m of the basin fill has been dated to the last 0.87 My. Throughout the basin, from proximal to distal locations, the late Quaternary succession of the Po Basin fill is characterized by vertical cyclic changes in facies, with channel stacking-patterns reflecting the Middle-Late Pleistocene alternation of glacial and interglacial periods (Amorosi et al., 2008, 2004, 1999a). Beneath the coastal sector, two wedge-shaped, coastal to shallow-marine sediment bodies, identified around ~100 m and 30 m depth (Fig. 2b) have been assigned to MIS 5e and MIS 1 respectively (Amorosi et al., 2004; Ferranti et al., 2006). Close to the Apennine margin and beneath the modern Po River, sheet-like fluvial channel-bodies were formed during glacial periods, which alternate with mud-dominated intervals assigned to the interglacials (Amorosi et al., 2008).

3. Materials and methods

3.1 Stratigraphic dataset

The study area is a ~8,500 km² wide sector of the Po Plain, framed between the cities of Mantova, Ferrara, Reggio Emilia, Bologna, and Rimini (Fig. 3). The stratigraphic reconstruction of the Late Pleistocene-Holocene succession – with a thickness of up to 150 m - has been carried out through the analysis and interpretation of a large stratigraphic dataset (Fig. 3), mostly recovered as part of the geological mapping (CARG) project of Italy (scale 1:50,000).

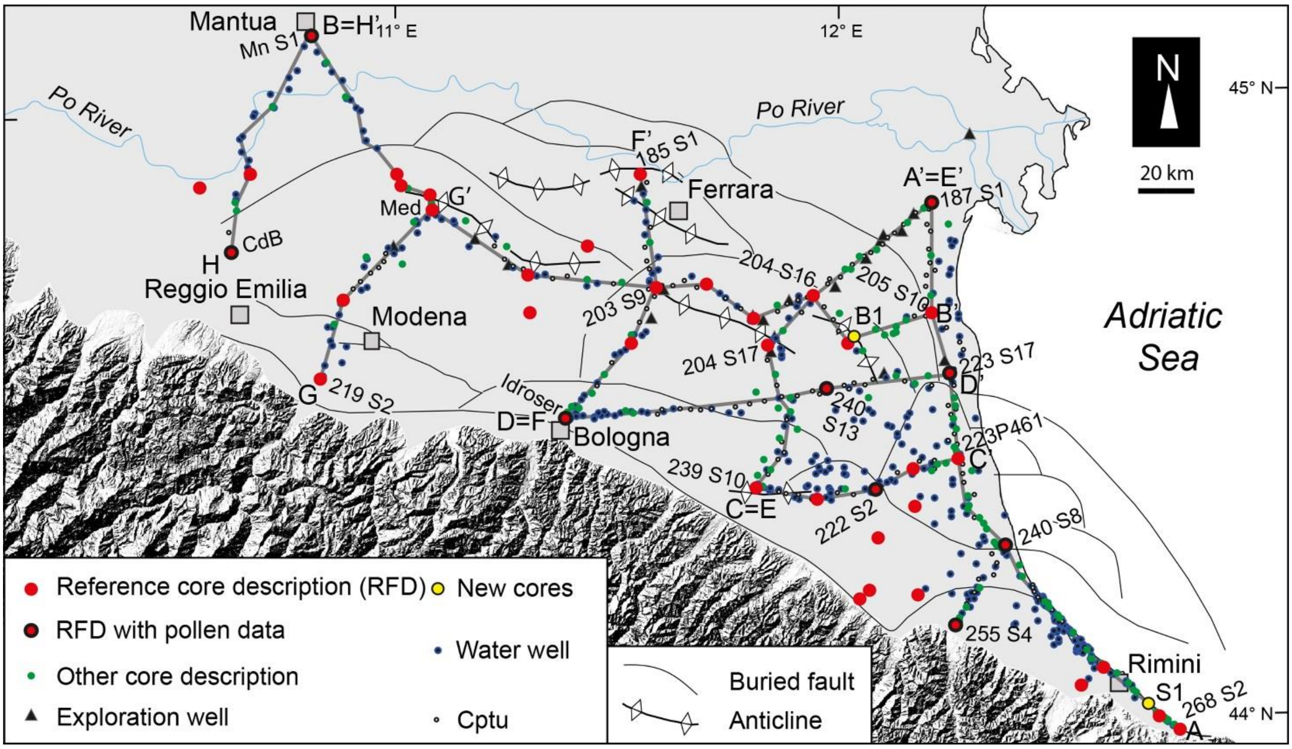

Fig. 3 – Study area, with indication of stratigraphic data used in this study and the main buried Apennine structures. Traces of cross sections of Figures 6-8 are represented by gray lines.

Stratigraphic data were provided by the geological surveys of Regione Emilia-Romagna and Regione Lombardia, and consist of 160 continuous-core descriptions, 554 water-well logs, 21 hydrocarbon exploration-well reports and 141 piezocone tests (see Data Availability). .

Descriptions from cores reaching depths of 30-200 m (Fig. 3), provide high-quality information about lithology, grain size, color, pedogenic and other featuressuch as peat layers, shell fragments, bioturbation, carbonate nodules, wood, and plant remains. Pocket penetration test values are frequently available. Selected core descriptions are part of published studies (Amorosi et al., 2008, 2004, 2001, 1999a; Bondesan et al., 2006; Castorina and Vaiani, 2018; Ferranti et al., 2006; Fiorini, 2004; Geological Map of Italy at 1:50,000 scale, Sheets: 256, 255, 241, 240, 223, 222, 221, 220, 205, 204, 187) and include sedimentological, micropaleontological, palynological and chronological data (i.e. ^{14}C and electron-spin resonance "ESR"; see Table 1 in Appendix and Data Availability). Among these, 44 cores with depths of > 100 m, have been used as reference (Fig. 3) for the identification of MIS 5e deposits and for detailed characterization of the post-MIS 5e succession.

Two continuously-cored boreholes (S1 and B1; see Fig. 3 for location), penetrating the entire MIS 5e-MIS 1 succession, were recently recovered close to the Apennine margin (core S1) and above the crest of a growing anticline in the Ferrara coastal plain (core B1; Fig. 3). Water wells (average depth ~ 150 m; Fig. 3) provided mostly basic lithological information (sand vs mud). Occasionally, the presence of marine shells is reported.

Hydrocarbon-well reports (average depth ~ 500 m; Fig. 3) provide the lowest-resolution stratigraphic information. Nevertheless, they offer petrophysical data that can be useful for lithological distinctions and, in a few cases, information about fossil and organic matter content is provided. Given their limited depth (< 35 m), piezocone tests (CPTU; Fig. 3) were utilized for stratigraphic correlation of the uppermost Pleistocene-Holocene (MIS 3-MIS 1) deposits. The reader is referred to Amorosi and Marchi, (1999), Amorosi et al., (2015) and Campo et al. (in press) for stratigraphic interpretation of CPTU tests.

3.2 Luminescence and radiometric dating

One undisturbed sample was collected from core B1 and sent to the Oxford Luminescence Dating Laboratory (University of Oxford, UK) for Optically Stimulated Luminescence (OSL) dating. This sample was recovered during drilling operations with an Osterberg cell from a depth of 39.9-39.3 m. The 60 cm core segment was removed and the exposed top and bottom parts were sealed with paraffin. Paraffin caps were removed in a dark room and the upper and lowermost ~5 cm of the sample were discarded. The innermost part of the core segment (39.85-39.5 m depth) was in turn split into four samples stored in lightproof containers and sent to the laboratory. At the laboratory, the samples were given the following laboratory codes:

i) X7339 (OSL sample), from core B1 (39.60-39.50 m depth);

ii) X7340 (OSL spare sample), from core B1 (39.75 m depth);

iii) X7341 (dosimetry sample), from core B1 (39.80 m depth);

iv) X7342 (dosimetry sample), from core B1 (39.85 m depth).

The resulting age is based on luminescence measurements of sand-size quartz (150-255µm) extracted from the samples using standard preparation techniques including, wet sieving, HCl (10%) treatment to remove carbonates, HF treatment (48%) to dissolve feldspatic minerals and heavy mineral separation with sodium polytungstate. Measurements were performed on small multigrain aliquots (n=30) with standard automated luminescence readers made by Risø (Bøtter-Jensen, 1997, 1988; Bøtter-Jensen et al., 2000) and Freiberg Instruments (Richter et al., 2015) using a double SAR post-IR blue or post-IR green OSL measurement protocol (Banerjee et al., 2001; Murray and Wintle, 2000; Wintle and Murray, 2006). Dose rate calculations are based on Aitken (1985) and are derived from the concentration of radioactive elements (potassium, rubidium, thorium and uranium) within the sediment sample. These were derived from elemental analysis by ICP-MS/AES using a fusion sample preparation technique. The final OSL age estimate includes an additional 4% systematic error to account for uncertainties in source calibration and measurement reproducibility. Dose rate calculations were obtained using dose rate conversion factors of Guérin et al. (2011) and calculated using the DRAC software (v1.02) developed by Durcan et al. (2015). The contribution of cosmic radiation to the total dose rate was calculated as a function of latitude. Altitude, burial depth and an average over-burden density of 1.9 g/cm^3 is based on data by Prescott and Hutton (1994).

Two organic-rich samples were collected from core B1 for radiocarbon analysis. Samples were dried at 40 °C and underwent to acid-alkali-acid pretreatment before AMS counting at KIGAM Laboratory (Korea Institute of Geoscience and Mineral Resources, Daejeon, Republic of Korea). OxCal 4.2 (Ramsey and Lee, 2013) with the IntCal 13 curve (Reimer et al., 2013) was used for radiocarbon age calibration.

4. Depositional facies associations

The complete MIS 6-MIS 1 succession of the southern Po alluvial and coastal plain was penetrated by cores S1 and B1, respectively 55 m and 39.9 m in length (Fig. 4). Lithofacies assemblages have been extensively described in previous studies and will not be reiterated here in detail. For detailed facies analysis of the MIS 6-MIS 3 interval, the reader is referred to Amorosi et al. (2008, 2004, 2001, 1999a) and Bondesan et al. (2006); whereas, for the MIS 2-MIS 1 interval, high-resolution facies descriptions have been reported by Amorosi et al. (2017a, 2017b), Bruno et al. (2017), and Campo et al. (2017). As documented by these studies, a large variety of facies associations typifies the MIS 6-MIS 1 Po Plain succession. For a complete overview of their major characteristics the reader may refer to the table in the Appendix. A generalized description of these deposits is given below. Twenty-one facies associations were grouped into five main depositional systems. Each group is briefly described from proximal to distal locations.

- Alluvial plain deposits. Three main facies associations form the alluvial plain depositional system: the fluvial-channel facies association is 2-30 m thick, and consists of fine to coarse sand, up to gravel bodies with fining-upwards (FU) trends (Fig. 4) and erosional lower boundaries. Crevasse and levee facies are made up of < 2 m thick sand bodies and sand-silt alternations, respectively (Fig. 4), with scattered root fragments. FU trends and sharp lower boundaries are characteristic of crevasse channels; in contrast, crevasse splays show coarsening-upward (CU) grain-size trends and gradational lower boundaries. The well-drained floodplain facies association is characterized by rooted and bioturbated clay and silty clay deposits with brownish mottles. Pedogenic features typical of weakly developed paleosols (Inceptisols; Fig. 4) are common. The occurrence of meiofauna commonly is rare, and includes fragments of freshwater (F) ostracods and poorly-preserved marine foraminifers, mostly sparse in sandy deposits. Freshwater gastropods are locally encountered (Fig. 4).

- Freshwater and organic-rich inner/wave-dominated estuarine deposits. This depositional system includes five freshwater (F), hypoaline and locally organic-rich facies associations (Fig. 4). Distributary-channel (Fig. 4) and related crevasse/levee facies associations share several characteristics with their alluvial counterparts: i.e. lithology, grain-size trends and erosional to transitional lower boundaries. However, distributary-channel deposits are thinner and generally finer-grained than fluvial-channel sand bodies. The bay-head delta facies association resembles distributary-channel sands in terms of lithology and sedimentary structures, but the abundance of plant debris, the local development of CU trends, and the association between freshwater and brackish fossils may represent diagnostic features. The poorly-drained floodplain facies association consists of gray clay and silty clay, with no pedogenic features (Fig. 4) and rare carbonate concretions. The swamp facies association is characterized by dark to brown clay, with abundant peat, wood fragments, and vegetal remains (Fig. 4). Pedogenic features are almost absent, with the only exception of histosols. The concentration of freshwater ostracods progressively increases from poorly-drained floodplain to swamp facies. Pocket penetrometer values (Fig. 4) have commonly been used for the differentiation of fine-grained deposits within the MIS 2-MIS 1 succession (e.g. well-drained floodplain, poorly-drained floodplain, and swamp clays, see Amorosi et al., 2015). This approach, however, can locally be adopted even for their older (MIS 6 to MIS 3, Fig. 4) counterparts, when they are not already overconsolidated.

- Brackish outer wave-dominated estuarine deposits. This depositional system is composed of four mud-dominated facies associations, with a diagnostic brackish fauna (B in Fig. 4), which is tolerant to sudden changes in salinity and organic matter content. Facies subdivision is based on (i) the frequency and thickness of sand intercalations, both increasing seawards; (ii) ostracod and foraminifer associations that reflect an increasing marine water influence downstream; (iii) organic matter concentration that increases landwards. From proximal to distal locations, brackish facies associations correspond to the following sub-environments: salt-marsh, mud-flat, central lagoon/bay and outer lagoon/bay.

- Transgressive barrier, strandplain, and delta front deposits. This depositional system includes four facies associations characterized by a generally high sand content. Grain size, ~~set (?)~~ thickness range, facies boundaries, and fossil content are the main diagnostic features: the transgressive sand-sheet facies association is the result of the shoreface retreat during MIS 5e-MIS 1 transgressions, and consists of shell-rich, medium-to-silty sands with a maximum thickness of 2 m, an erosional lower boundary and FU trends; the upper shoreface/foreshore facies association includes medium to coarse sand-bodies (1-5 m thick), with a gradational lower boundary; the lower shoreface facies association also shows transitional lower boundaries to the underlying prodelta facies and is composed of fine to very fine sand-bodies, 1-5 m thick; the mouth bar facies association, up to 10 m thick, includes medium to fine sand deposits, with an abundance of plant debris (Fig. 4). The transgressive sand-sheet facies includes reworked sediments, with a reworked microfauna and an abundance of mixed marine and brackish mollusk species (R in Fig. 4). Within mouth-bar and upper shoreface/foreshore facies, no foraminifers or ostracods are generally preserved and a paucity of shells is recorded. On the contrary, an abundant and highly diverse marine fossil assemblage (M in Fig. 4) is typical of nearshore facies: i.e. especially lower shoreface.

- Offshore/prodelta deposits. This mud-dominated depositional system represents the most distal portion of the Po Basin succession recovered onshore. Five facies associations were grouped into this depositional system. All these facies include marine (M) fossils assemblages. Fine sand-clay alternations are characteristic of the most proximal facies associations, such as the delta-front transition and offshore transition deposits. These facies associations accumulated in similar water depths but in different subenvironments characterized by high (i.e., delta-front transition) vs low/none (i.e., offshore transition) river influence, as the distance from the river mouth increases. Delta-front transition facies may include plant debris. Seawards, the sand/mud ratio rapidly decreases and organic-matter content increases: proximal prodelta facies (silty clay) is progressively replaced by distal prodelta facies (clay), up to 8 m thick. The offshore facies association is made up of bioturbated clay deposits, up to 2 m thick. The highly diversified meiofauna, typical of open-marine conditions, and lithological characteristics are consistent with the relatively deep depositional environment. Offshore-transition deposits are characterized, instead, by less diversified assemblages; whereas, prodelta muds generally include opportunistic species able to tolerate stressed marine conditions (i.e. high freshwater and sediment inputs) related to river floods.

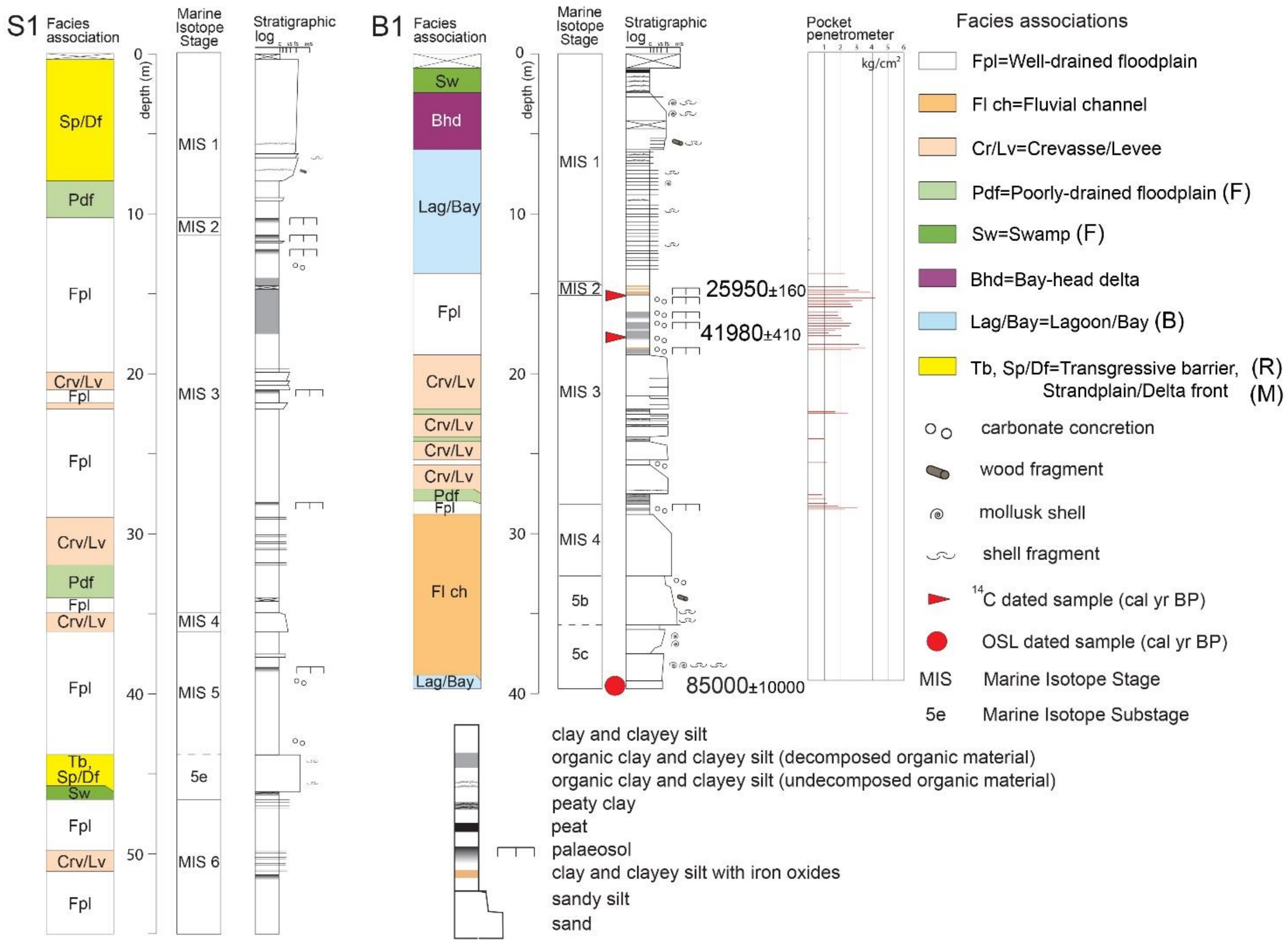

Fig. 4 – Stratigraphic log and facies associations from cores S1 and B1. Location in Figure 3. F: freshwater; B: brackish; R: reworked; M: marine.

5. Pollen-based stratigraphic correlations

Stratigraphic correlations relied upon the combination of facies and pollen data available for 9 cores (Fig. 3). Particularly pollen data provided important information about climate-related vegetational and environmental changes.

Pollen taxa subdivision follows their ecological and climatic affinities (i.e. arboreal vs non arboreal and warmth- vs cold-loving taxa; see Zangheri, 1976; Pignatti, 1998, 2017), as previously done by Amorosi et al.

(2008, 2004, 2001,1999a). Two main groups have been distinguished: arboreal (AP) and non-arboreal pollen (NAP). AP can be subdivided into three components: (i) *Quercus* group, representative of warm-temperate phases (interglacials), which includes humidity- and warmth-loving species of deciduous broad-leaf forests dominated by oaks; (ii) mountain trees and (iii) *Pinus* which are indicative of cool-wet and cold climate conditions (glacials), respectively. NAP (i.e. shrubs and herbs), withstanding dry conditions, are indicators of cold steppic environments.

Vertical changes in facies associations and pollen spectra led to high-resolution stratigraphic correlations and subdivision into sediment units deposited during specific Marine Isotope Stages. Basin-scale correlations between three reference cores, representative of proximal (core Mn S1), intermediate (core 203 S9), and distal (core 223 S17) locations of the Po Basin are shown in Figure 5. A schematic stratigraphic log with facies interpretation is provided for each core. Detailed palaeontological analyses are available for cores 203 S9 and 223 S17 (Geological Map of Italy at 1:50,000 scale, Sheet: 203; Amorosi et al., 1999a), whereas pollen data were obtained from cores Mn S1, Idroser (projected on core 203 S9) and 223 S17 (Amorosi et al., 2008, 2001, 1999a).

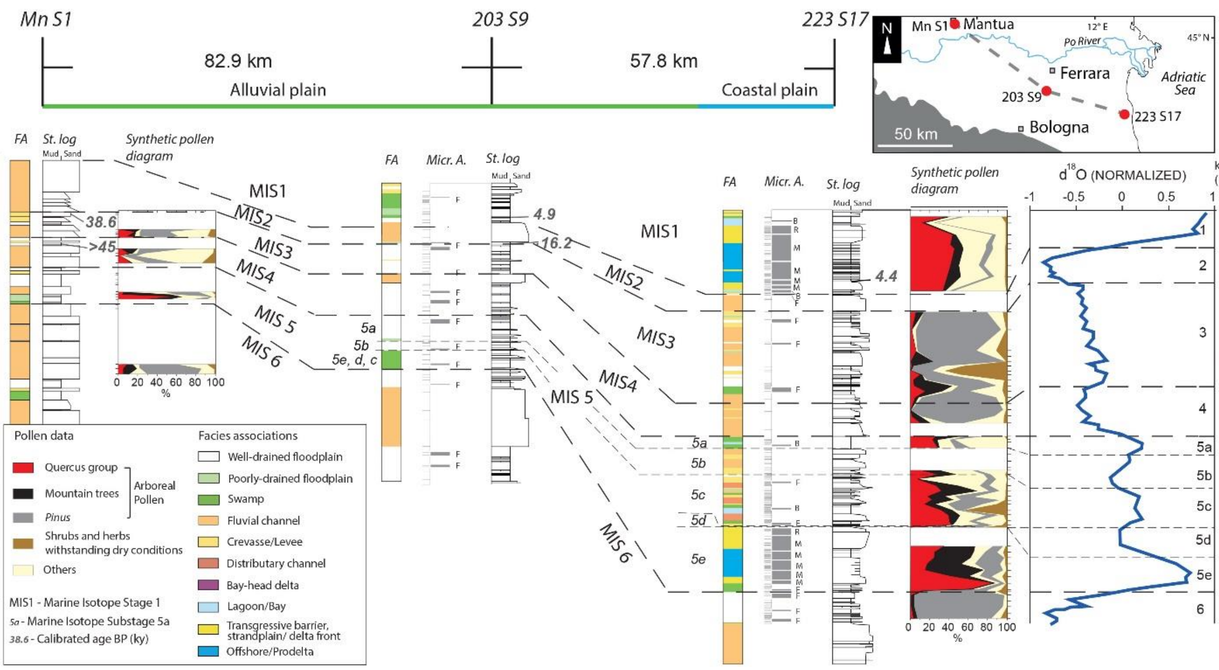

Fig. 5 –Basin-scale correlation from proximal (alluvial plain) to distal (coastal plain) locations of the Po Basin. Facies associations and pollen signals recorded from cores were correlated with the oxygen-isotope ($\delta^{18}O$) record of the last 150 ky (blue line; modified from Martinson et al., 1987). FA: facies association; St. log: stratigraphic log; Micr. A.: Micropaleontological association (F: freshwater; B: brackish; R: reworked; M:

marine). See Figure 3 for location of the cores, and Table A1 (Appendix) for details on radiocarbon dates. For the original pollen data the reader may refer to Data Availability.

As pollen concentration is very scarce in sandy deposits, the pollen curve from core Mn S1 is highly discontinuous (Amorosi et al., 2008). However, pollen profiles from cores Mn S1, 203 S9 (i.e., Idroser) and 223 S17 show comparable pollen spectra at specific stratigraphic intervals (Fig. 5). Peaks in *Quercus* highlight the onset of warmer/temperate periods on a basin scale. Two major warm phases were identified and linked to the major peaks in $\delta^{18}O$ during MIS 5e and MIS 1 (Martinson et al., 1987, Fig. 5). The transition from glacial to interglacial periods (e.g., MIS 6/5e) is characterized by sharp changes in pollen taxa (Fig. 5; Amorosi et al., 2004) from high *Pinus* and mountain trees percentages (cold indicators) to high *Quercus* percentages (warm indicators).

Pollen variations at glacial/interglacial transitions are paralleled by abrupt facies variations that reflect rapid sea-level rise (Fig. 5). As an example, well-drained floodplain muds assigned to the MIS 6 glacial are typically overlain by interglacial paralic and coastal facies associations attributed to MIS 5e (Fig. 5). Landwards of the line of maximum marine ingression (core Mn S1, Fig. 5), the same pollen signal is associated with the abrupt shift from barren fluvial sands to overlying (“transgressive”) swamp muds.

The correlation of stages and substages relies upon similar changes in pollen signals and on vertical stacking patterns of facies, with an additional contribution by radiocarbon ages for the MIS 3-MIS 1 interval (Fig. 5). Minor transgressions correlate with minor peaks in $\delta^{18}O$ (MIS 5c and 5a in Fig. 5). The thick alluvial succession sandwiched between MIS 5e and MIS 1 deposits, and mostly characterized by cold pollen signatures can be assigned to MIS 4-3-2 (Fig. 5). Poorly-drained and swamp deposits within this interval may reflect lower magnitude transgressive pulsations mostly recorded at the onset of MIS 3 (Fig. 5).

6. MIS 5e-MIS 1 stratigraphy in the southern Po Basin

Basin-scale correlations along eight stratigraphic transects (Figs. 6-8) document the high-resolution, Late Pleistocene-Holocene facies architecture of the Po Plain. Pollen data, coupled with ESR, OSL and radiocarbon ages enable age attribution of the investigated strata, and their assignment to the MIS 5e-MIS 1 interval.

Two > 100 km-long stratigraphic transect were constructed: AA’ (Fig. 6a) extends from the Apennine margin to the modern Po Delta and is approximately parallel to the modern shoreline; and BB’ (Fig. 6b) which runs parallel to the Apennine margin, extends from the town of Mantua to the Adriatic coast (Figs. 3, 6). Figure 7 includes three stratigraphic cross-sections (i.e. CC’, DD’ and EE’) that were traced in the distal sector of the study area. The south-north oriented stratigraphic transects of Figure 8 (i.e. FF’, GG’, HH’) were constructed to explore along-strike changes in stratigraphy at proximal locations.

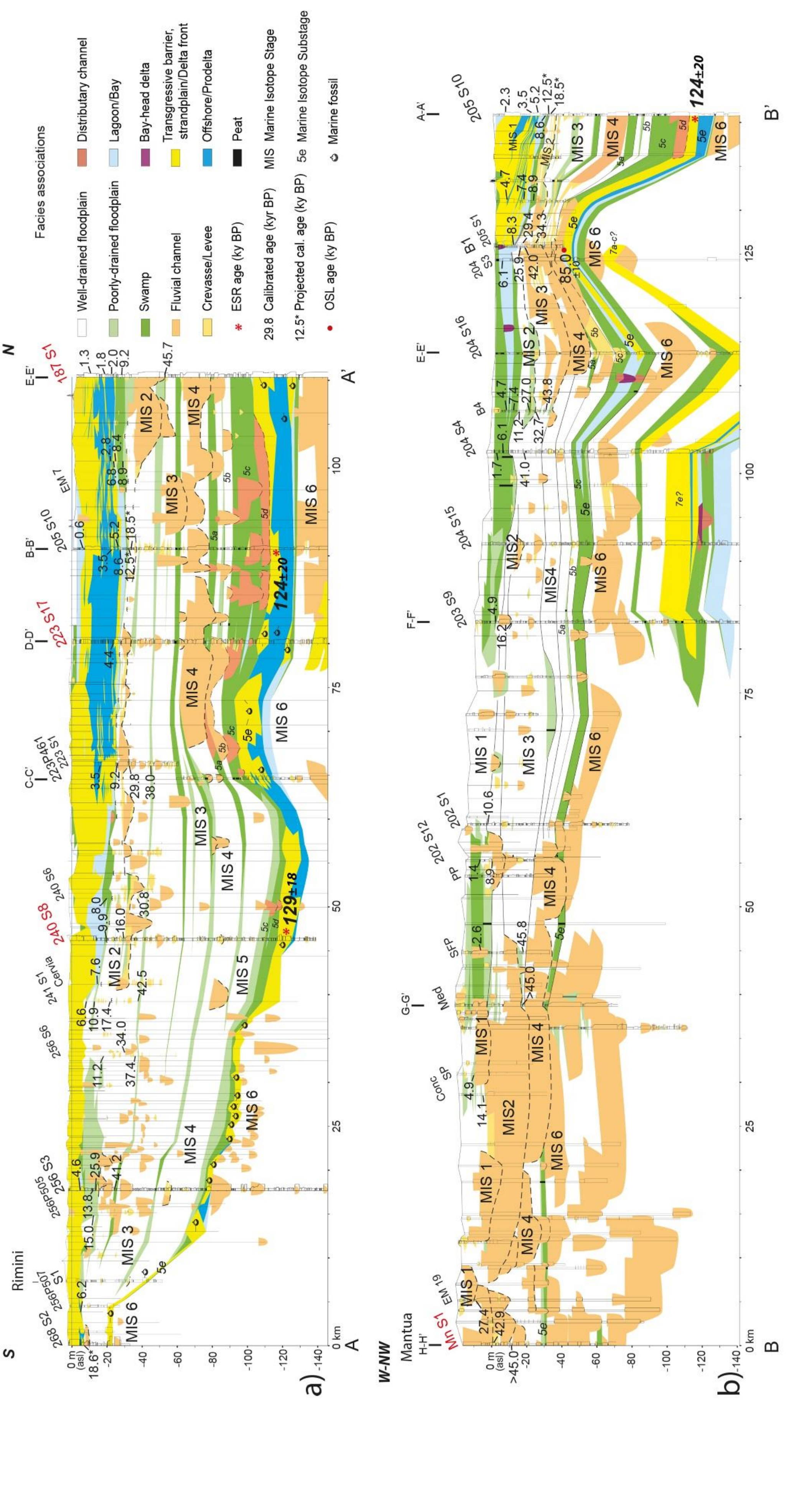
Facies associations
Well-drained floodplain
Poorly-drained floodplain
Swamp
Fluvial channel
Crevasse/Levee
ESR age (ky BP)
29.8 Calibrated age (kyr BP)
12.5* Projected cal. age (ky BP)
OSL age (ky BP)
Distributary channel
Lagoon/Bay
Bay-head delta
Transgressive barrier, strandplain/Delta front
Offshore/Prodelta
Peat
MIS Marine Isotope Stage
5e Marine Isotope Substage
Marine fossil
a)
b)
S
N
W-NW
Rimini
Mantua
A
A'
B
B'

Fig. 6 – Basin-scale stratigraphic architecture of the MIS 5e-MIS 1 succession of the Po Basin along two stratigraphic panels oriented parallel to the modern shoreline (a) and to the Apennine margin (b), respectively. See Figure 3 for location and Table A1 (Appendix) for details on radiocarbon dates. In red, reference cores with pollen data (see Data Availability).

The Last Interglacial (MIS 5e) coastal wedge, encountered at depths between 130 and 20 m, represents a prominent stratigraphic marker in the late Quaternary succession (Fig. 6). It is marked at the base by a characteristic deepening-upward trend, with transition from swamp to lagoon/estuary and transgressive-barrier facies (see cores 223 S17, 205 S10, 187 S1; Fig. 6a). In the distal sector, these deposits are overlain, in turn, by offshore and prodelta muds (Figs. 6 and 7). The prodelta facies association is overlain by a laterally extensive (> 100 km), ~10 m-thick, sand sheet made up of strandplain and delta front facies (Figs. 6 and 7). MIS 5e coastal deposits wedge-out southwards (Fig. 6a) and also towards the west (Fig. 6b), where coastal sands (cores 205 S10-204 S16) are progressively replaced by thin lagoon (core 204 S4) and swamp (cores 204 S15 and Mn S1) deposits. Close to the Apennine margin, where the MIS 5e succession is composed entirely of alluvial deposits (Figs. 7 and 8), lacking pollen data, the MIS 6-5e boundary has been tentatively placed in correspondence of a paleosol (core 239 S10; Fig. 7a, c) or atop laterally extensive fluvial-channel gravels, (core 219 S2; Fig. 8b). The top of MIS 5e deposits, generally ranging between 120 and 100 m depths, is only 60-40 meters deep at the top of the buried anticlines (Figs. 6b, 7b, c; Fig. 3 for location). Locally, MIS 5e deposits have been partially (Fig. 6a) or completely (Fig. 6b) eroded by younger fluvial/distributary-channel deposits. For example, in core B1, the OSL date from a distributary-channel deposit above MIS 5e marine sands yielded an age of 85±10 ky BP (Figs. 4 and 6b), consistent with a MIS 5a to MIS 5c age attribution (Otvos, 2015).

A thick (up to 95 m) succession made up entirely of non-marine deposits overlies the MIS 5e coastal wedge (Fig. 6). It is characterized by a cyclic alternation of swamp and locally brackish (core 223 S17) deposits with alluvial facies, showing an overall shallowing-upward trend. Two thin lagoon horizons have been identified between 90-65 and 60 m depth (Fig. 7b). Paludal deposits can be tracked landwards for about 40 km (Fig. 6b). Their thickness and lateral extent decrease upsection and southwards (Fig. 6a). Similarly, poorly-drained floodplain intervals thin out upstream where they are progressively replaced by well-drained-floodplain muds and fluvial-channel sands (Figs. 6b, 7a, b). Three laterally extensive (> 40 km) fluvial channel-belt sand bodies, up to 20 m thick, are vertically stacked in the northern sector, between 80 and 30 m depths (Fig. 6a). The deepest sand sheet has been tentatively assigned to MIS 4. The narrower (< 15 km, Fig. 6b) and thinner (~ 5 m) fluvial-channel sand body accumulated between 45 and 30 ky BP (see radiocarbon dates in Fig. 6 and Table 1). The deposition of the youngest fluvial channel-belt took place between ~ 30 and 12 ky BP (Fig. 6).

The uppermost stratigraphic interval is the Holocene coastal wedge, that was deposited during the last 10 ky BP (radiometric ages of Figs. 6-8). It shares many characteristics in terms of facies distribution and geometry of sediment bodies with its MIS 5e counterpart (Fig. 6). Similarly, it wedges out toward the west (Fig. 6b), with a landward transition from marine to alluvial deposits. A comparable upward transition from basal estuarine deposits to a laterally extensive (> 100 km) coastal sand-sheet (Fig. 6a) typifies the early Holocene succession. Middle-late Holocene deposits, however, display thicker prodelta and strandplain/delta front deposits. (Fig. 6a). The maximum upstream migration of swamp, lagoon and coastal facies associations is less pronounced for the Holocene coastal wedge than for MIS 5e deposits (Figs. 6b, 7a, b, 8a).

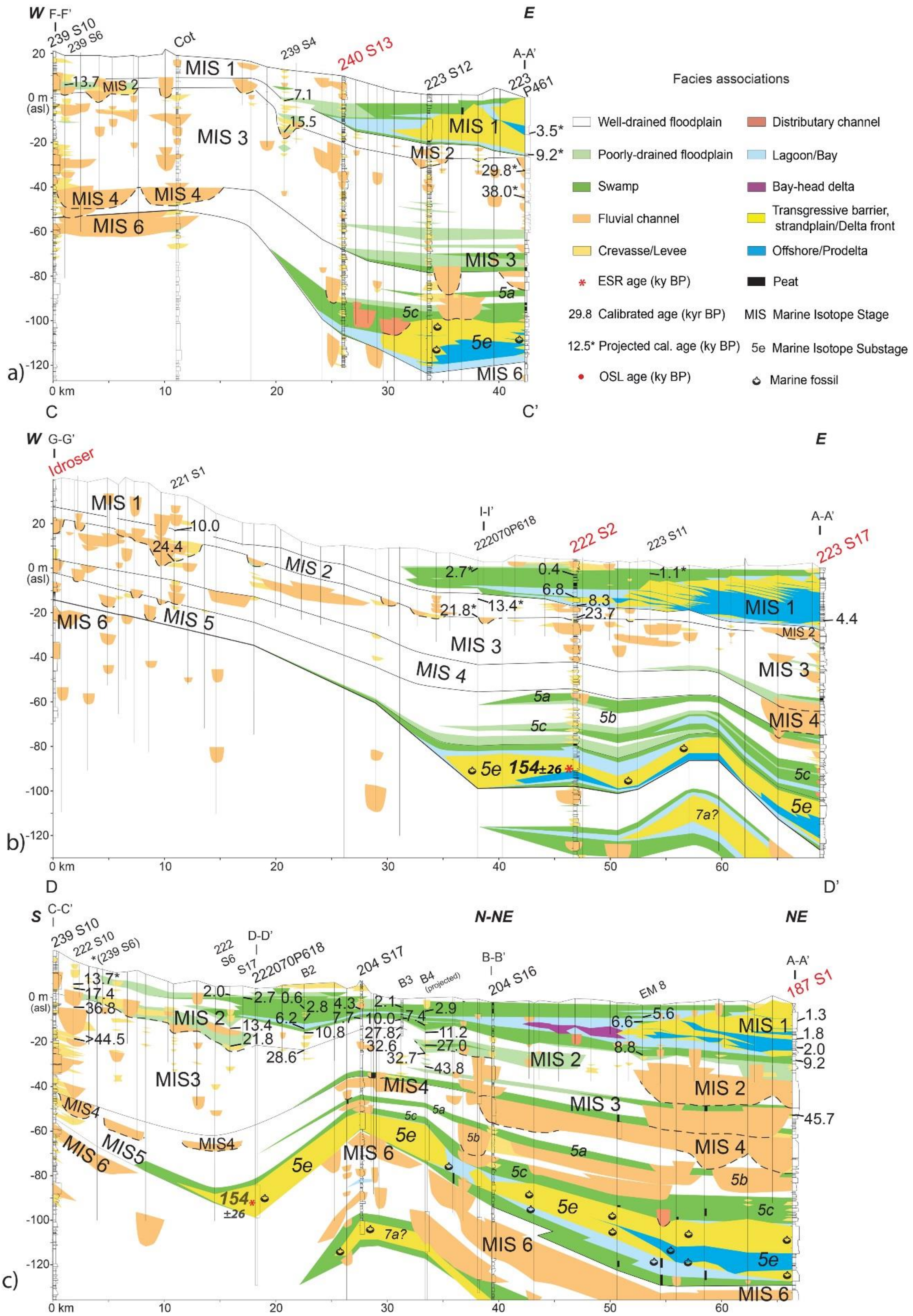

Fig. 7 – MIS 5e-MIS 1 stratigraphy of the Po Basin at distal locations. a) Stratigraphic panel CC'. b) Stratigraphic panel DD'. c) Stratigraphic panel EE'. See Figure 3 for location, Figure 6 for legend and Table 1 (Appendix) for details on radiocarbon dates. In red, reference cores with pollen data (see Data Availability).

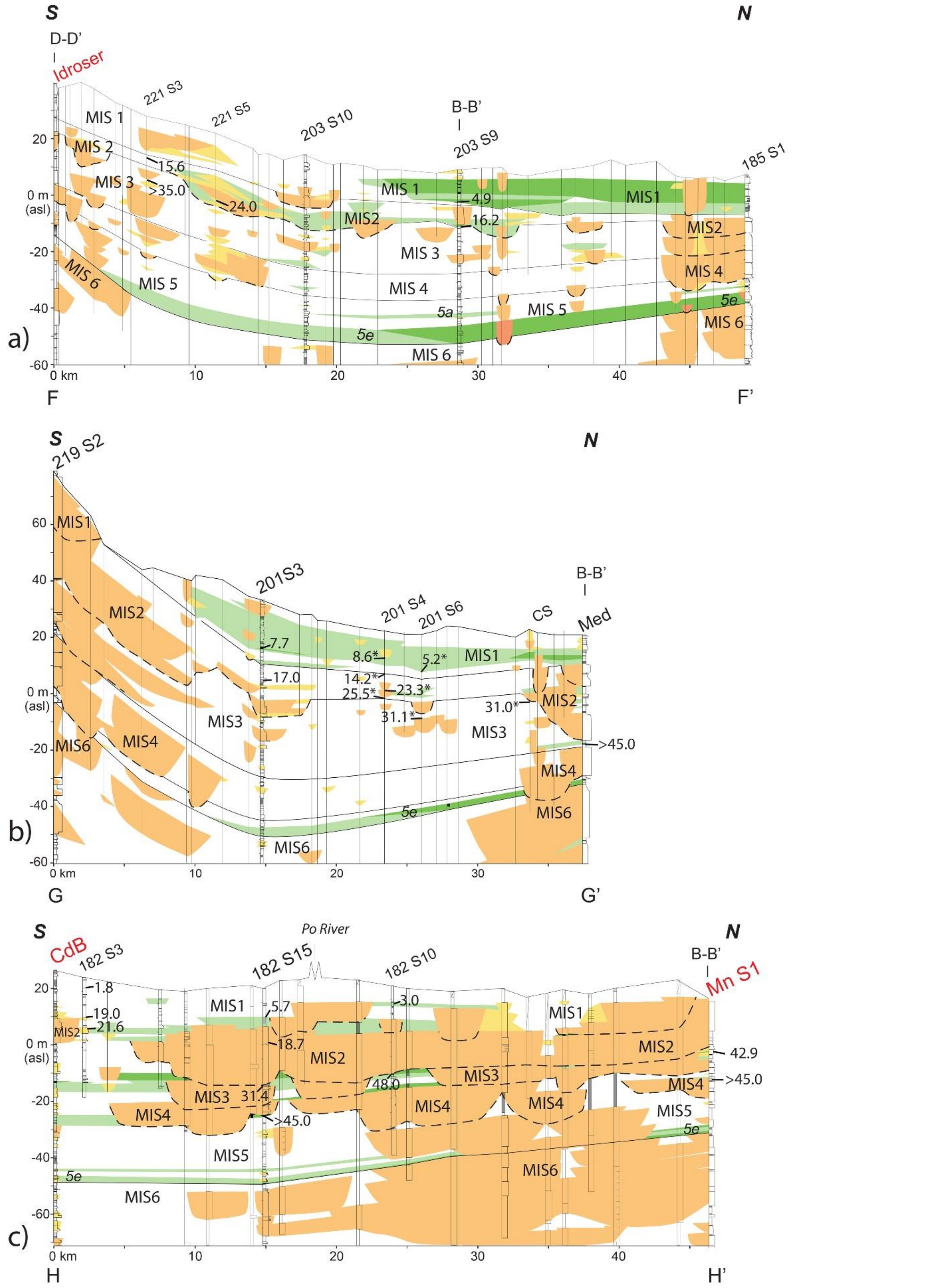

Fig. 8 – MIS 5e-MIS 1 stratigraphy of the Po Basin at proximal locations. a) Stratigraphic panel FF'. b) Stratigraphic panel GG'. c) Stratigraphic panel HH'. See Figure 3 for location, Figure 6 for legend and Table 1 (Appendix) for details on radiocarbon dates. In red, reference cores with pollen data (see Data Availability).

7. Factors controlling sediment deposition and preservation

7.1 Eustatic control on MIS 5e-MIS 1 stratigraphy

Facies and vegetation changes at the MIS 6/5e transition clearly reflect post-glacial sea-level rise (Waelbroeck et al., 2002). Since global mean surface temperatures were at least 2° C warmer than at present, the mean MIS 5e sea-level stood 4-6 m higher than the modern sea-level (Rohling et al., 2008), with oscillations up to 9 m (Dutton and Lambeck, 2012; Kopp et al., 2013; Rovere et al., 2016). Consequently, many coastal areas worldwide experienced the effects of a severe marine ingression (Bardají et al., 2009; Mauz et al., 2012; Murray-Wallace et al., 2016; Otvos, 2015; Peeters et al., 2019; Törnqvist et al., 2000). In the southern part of the study area (south of Ravenna in Fig. 9), the MIS 5e and MIS 1 (i.e., modern) shoreline positions approximately coincide. This is possibly due to the high topographic gradient at the basin margin that likely hindered marine transgression. On the contrary, SE of Ferrara the MIS 5e shoreline backstepped up to 36.5 km landwards of the modern beach position (9.5 km west of its MIS 1-highstand analogue - Fig. 9). Brackish lagoonal and outer estuarine environments extended up to 47.5 km from the modern shoreline, whereas more or less continuous freshwater swamp, inner-estuary environments are recorded up to 140 km upstream of the present-day coastline (Fig. 9). Poorly-drained and well-drained floodplain facies associations characterize the more abrupt transition from coastal to alluvial settings towards the Apennine margin (Fig. 9). This reconstruction is consistent with the work of Fontana et al. (2010), who placed the inner margin of the MIS 5e lagoon 10-20 km landwards of the Holocene one, in the nearby Venetian-Friulian coastal Plain.

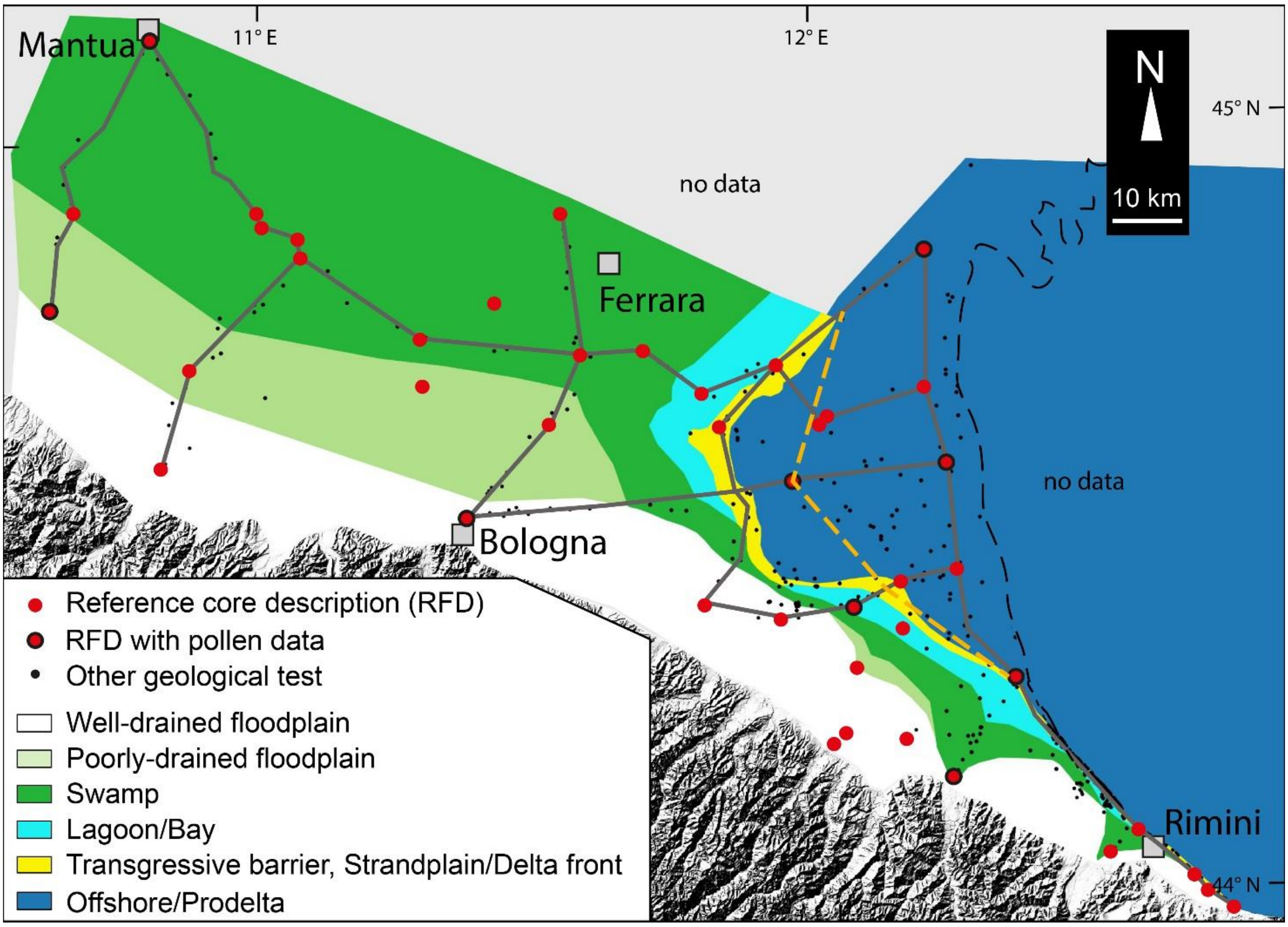

Fig. 9 – Paleogeography of the Po Plain during the MIS 5e maximum marine ingression. Gray lines indicate the traces of stratigraphic panels of Figures 6, 7, 8. The orange dashed line depicts the MIS 1 shoreline during the MIS 1 maximum marine ingression. The black dashed-line indicates the modern shoreline.

The correlation of cyclic facies patterns and pollen signals with the oxygen-isotope record of the last 150 ky (Fig. 5) testifies to a major glacio-eustatic control on MIS 6-MIS 1 stratigraphic architecture in the Po Basin. At the scale of the last interglacial-glacial cycle (~10^5 years), in fact, the contribution of other allogenic (e.g., tectonics) or authogenic controlling factors on facies architecture is less clear and/or significant. Authogenic component, for example, seems to play a key-role at smaller (parasequence, 10^2-10^3 years) scale, as documented by Amorosi et al. (2017, 2019). On the other hand, the exceptional stratigraphic expansion of the Po sedimentary infill, due to the high subsidence rates, allows preservation of the whole suite of Marine Isotope Stages (5 to 1) and, locally, even substages (5e-a; Figs. 6-7-8). Natural subsidence consists of a long-term component (tectonics, geodynamics, sediment load and compaction) and a short-term component due to deglaciation effects (Carminati et al., 2003, 2005). Identification of glacial and hydro-isostatic adjustment component in the Mediterranean region is difficult though, especially in correspondence of major river deltas (such as the Po River delta) where subsidence caused by sediment loading and compaction strongly affects the relative sea level record (Vacchi et al., 2018). However, Spada et al. (2009) realized a model showing that, south of the Po River, the post-LGM melting of the Alpine ice sheet reduced the sea-level rise generated by the melting of the remote ice-sheet in the far-field of the Mediterranean alone. This result matches with other studies (Vacchi et al., 2016; Antonioli et al., 2009) supporting a dominant role of the long-term geological component of vertical deformation upon the isostatic terms in the southern Po Plain.

Apart from the two major transgressive pulsations, clearly marked by the two (MIS 5e and MIS 1) coastal wedges, thin brackish and organic-rich intervals (Figs. 6-8) are interpreted to reflect minor transgressions (i.e. MIS 5c, 5a, MIS 3) within the general sea-level fall that characterized the MIS 5e-MIS 2 interval. This interpretation is supported by: the i) OSL age on B1 core, dating the first non-marine sands between MIS 5c and MIS 5a (Figs. 4-6b); and the ii) pollen associations from these horizons, which invariably suggest phases of general climate amelioration. On the contrary, the fully alluvial MIS 5d and 5b stratigraphic intervals are associated to pollen assemblages typical of colder conditions. This trend has also been observed in the Rhine-Meuse system (Busschers et al., 2005; Peeters et al., 2015) and the Gulf of Mexico coastal plain (Blum and Aslan, 2006; Otvos, 2005, 2013), where the re-establishment of alluvial settings is associated with the switch to glacial climatic conditions. MIS 4, 3 and 2 are almost entirely composed of alluvial facies (with the exception of a discontinuous, organic-rich interval assigned to MIS 3, Figs. 6-8), with pollen spectra dominated by *Pinus* and mountain tree taxa. Locally, peaks of shrubs and herbs (e.g., Fig. 5) likely suggest the episodic instauration of steppic environments. MIS 4 and MIS 2 intervals are characterized by two major fluvial channel belts, up to 30 m thick. These laterally extensive fluvial sand bodies are coeval with vertically-stacked paleosols (Figs. 6-8) that likely formed in response to abrupt sea-level falls at the transitions between MIS 5/4 and MIS 3/2, respectively (Waelbroeck et al., 2002). The vertical stacking of fluvial channel-belts contrasts with stratigraphy from several coastal plains worldwide, where stepped sea-level fall, down to -120 m at the onset of MIS 2 (Waelbroeck et al., 2002), led to the formation of well-developed incised-valley systems (Blum et al., 2013; Busschers et al., 2005; Hori et al., 2002; Milli et al., 2016; Peeters et al., 2016; Tanabe et al., 2013, 2006). This is likely due to high subsidence rates (~ 1 mm/y) in the Po Basin, associated with high volumes of sediment supplied by distinct Alpine and Apennine sources (Campo et al., 2016; Fontana et al., 2014).

7.2 Structural control on thickness distribution

The MIS 5e-MIS 1 Po Basin succession is characterized by an exceptional thickness (up to 130 m, Figs. 6-8). Coeval successions around the world do not provide such a highly-detailed continuous sedimentary record for the last 130 ky. For example, in the marine core MD95-2042 located off the southwest coast of Portugal (Sánchez Goñi et al., 1999), the thickness of the last 130 ky sedimentary record is about 26 m. In other sedimentary successions, only distinct stratigraphic intervals are well preserved. For example, Amorosi et al. (2014) documented an uninterrupted marine sedimentary record of MIS 5e, of just 8.5 m (Fronte section, southern Italy).

Relatively thick successions have been reported from the subsurface of modern subsiding basins. In the Versilian plain (central Italy), for example, MIS 5e-MIS 1 deposits are 72 m thick (Carboni et al., 2010). However, in most alluvial systems worldwide, Late Pleistocene-Holocene strata are generally poorly-preserved due to river incision driven by stepped post-MIS 5e sea-level fall (Blum et al., 2013; Blum and Törnqvist, 2000). In the Netherlands, the MIS 5e-MIS 1 succession is preserved only within incised valleys, with thicknesses ranging between 25-60 meters along-dip (Busschers et al., 2007; Peeters et al., 2016, 2015).

In the Po Basin, the MIS 5e-MIS 1 succession has also variable thickness along-dip, between 25 and 130 meters (Figs. 6-8), where minimum values are recorded close to Apennine margin (Fig. 6a). Comparable limited thickness is also observed close to the buried growing anticlines (Fig. 6b), where the MIS 5e coastal sands can be displaced up to 70 m (Fig. 6b), and the thickness of the post-MIS 5e succession can be as little as ~ 30 m. As a whole, the general thickness distribution of the post-MIS 5e interval clearly reflects the structural setting of the Po Basin, and thus the distribution of the NNE verging fold-and-thrust systems of the Apennines (Ghielmi et al., 2013). The effect on stratigraphy of the buried Apennine structures is clearly observed between cores 205 S10 and B1 (Figs. 6b and 7c), where the thickness of the post-MIS 5e succession changes abruptly from 127 m to 51 m in about 10 km (Fig. 6b). Similarly, a change in thickness of about 30 m is recorded between well 222070P618 and core 204 S17 (Fig. 7c).

Thickness variations and deformation of stratigraphic units that compose the Plio-Quaternary Po Basin fill have been observed in numerous seismic profiles (Pieri and Groppi, 1981). In this work a significant lateral variations in thickness and deformation of Late Pleistocene strata at the subseismic-scale (Figs. 6-8)has been documented. Based on the elevation of the MIS 5e coastal sands and the modern coastal deposits, subsidence rates have been calculated dividing the MIS 5e-MIS 1 sediment thickness for the time interval (i.e., 125 ky). During the last 125 ky, subsidence ranged between 0.20 mm/y, close to the Apennine margin (in proximity of the city of Rimini), and 1.05 mm/y between the city of Cervia and the modern Po Delta (Figs. 6-9). Since the structures of the Emilia and Ferrara Arcs are tectonically active (Amadori et al., 2019), it is very difficult to rule out the possible influence of recent tectonic activity on thickness distribution and deformation of Late Pleistocene strata, with a significant contribution of differential sediment compaction.

It is possible to speculate that certain thrusts were most likely already active during the deposition (i.e., syntectonic) of the MIS 5e-MIS 1 strata. Similarly, during the last 125 ky, the study area could have been hit by several major earthquakes. These events may provoke up to 17 cm anticlinal crest growth, as shown by InSAR data analysis after the 2012-earthquake (Caputo et al., 2015). On the other hand, the interplay between sedimentary processes and high-sedimentation rates could have exceeded the velocity of the growing structures (as documented by Carminati et al., 2010 for the Mirandola area) and temporarily cover the tectonic effect (and the potential erosion) on sedimentary bodies. For example, a relative tectonic uplift of 0.16 mm/y was calculated for the Mirandola anticline (Scrocca et al., 2007), whereas the velocity of backstepping-barrier systems or delta progradation during Holocene reached 10 and 15 m/y, respectively (Bruno et al., 2017; Amorosi et al. 2019 SED).

Preexisting or new (e.g., seismogenically) generated structural highs could also have been playing a key role (morpho-tectonic?) on sediment and facies distribution, as suggested by the abrupt landward replacement of Holocene beach-barrier deposits with thick lagoonal deposits between cores 204 S3 and B1 (Fig. 6b). Given the intrinsic complexity of the geological and structural framework and the interplay between all the processes acting at different time/intensity scales, additional investigations are needed to better define and quantify the role of neo-tectonics on the MIS 5e-MIS 1 deposits of the Po Basin.

Conclusions

Last Interglacial (MIS5e) coastal deposits represent a stratigraphic marker of worldwide significance that provides specific information about paleoclimate and paleo-sea level, and that can be used on a basin-scale to infer regional tectonics. MIS 5e strata have been reported from the subsurface of the Po Plain in several local studies, but basin-scale stratigraphic reconstructions have never been carried out. Based on 876 stratigraphic data (e.g. cores, well logs and piezocone tests), with the aid of micropaleontological, pollen, and chronological data (i.e. radiocarbon, ESR and OSL), regional stratigraphic correlation of MIS 5e deposits was established and the high-resolution facies architecture of the Late Pleistocene-Holocene succession was reconstructed with high stratigraphic detail.

The MIS 5e coastal wedge can be tracked continuously for > 100 km along strike and up to 140 km along dip. It includes the retrogradational stacking of paralic and coastal facies, overlain by prograding deltaic deposits. Coastal sands, up to 25 m thick, thin-out southwards and westwards, where they are progressively replaced by lagoon, swamp and alluvial facies.

The post-MIS 5e succession, dated between about 85 and 12 ky BP, exhibits an overall shallowing-upward trend due to the general sea-level fall: lagoon and swamp deposits are abundant atop the MIS 5e deposits, but they become thinner upsection, where alluvial facies are dominant. Stacked fluvial channel belts formed during MIS 4-2 due to the combination of high-subsidence rates and high-sediment supply. This overall trend reflects the stepped basinward shift of facies induced by sea-level drop, between MIS 5d and MIS 2. Brackish and swamp horizons are associated with minor transgressions (MIS 5c, 5a, MIS 3) within the general sea-level fall.

The Holocene (MIS 1) deposits record the post-LGM sea-level rise and subsequent Po-delta progradation under highstand conditions. The MIS 1 coastal wedge shares many characteristics in terms of pollen signals, facies trends, geometry and thickness of sedimentary bodies with its older (MIS 5e) counterpart. Due to higher global sea-level during the Last Interglacial, however, the MIS 5e shoreline reached a 9.5 km more landward position than maximum marine ingression during MIS 1: 36.5 km landwards of the modern shoreline.

The MIS 5e-MIS 1 succession displays an extremely variable thickness across the Po Basin. The exceptional thickness (~130 m) preserved in the depocenters makes the Po Plain succession one of the most extensive, continuous and highly-resolved stratigraphic records of the last 130 ky. The elevation of the MIS

5e stratigraphic marker changes dramatically on top of the major buried thrust fronts, where subsidence in the last 130 ky decreases from 1.0 to 0.2 mm/y.

Data Availability

- The download of geological tests used in this work is available only in Italian at the following links: https://applicazioni.regione.emilia-romagna.it/cartografia_sgss/user/viewer.jsp?service=geologia (Regione Emilia-Romagna; accessed august 2019); https://www.cartografia.servizirl.it/viewer32/index.jsp?config=config_caspita.json (Regione Lombardia; accessed august 2019).
- Pollen data are available from nine reference cores. For each core the source of data is provided:
  Core 187 S1: pollen data (only in Italian) at http://www.isprambiente.gov.it/Media/carg/note_illustrative/187_Codigoro.pdf, pages 132-133.
  Core 223 S17: pollen spectra published by Amorosi et al., 2004, 1999a.
  Core 240 S8: pollen spectra published by Amorosi et al., 2004.
  Core 255 S4: pollen spectra (only in Italian) at http://www.isprambiente.gov.it/Media/carg/note_illustrative/255_Cesena.pdf, p. 76.
  Core 222 S2: pollen spectra (only in Italian) at http://www.isprambiente.gov.it/Media/carg/note_illustrative/222_Lugo.pdf, p. 92.
  Core 240 S13: pollen spectra published by Amorosi et al., 2004.
  Core Idroser: pollen spectra published by Amorosi et al., 2001.
  Core CdB: pollen data (only in Italian) at http://www.isprambiente.gov.it/Media/carg/note_illustrative/200_Reggio_nellEmilia.pdf, pages 91-95.
  Core Mn S1: pollen spectra published by Amorosi et al., 2008.
- EPR ages for cores 205 S10, 222 S2 and 240 S8 published by Ferranti et al., 2006, page 45, their Table 2.
- Original radiometric ages from the Geological Map of Italy (only in Italian) at 1:50,000 scale (Geological Survey of Italy and CARG Project):

Sheet 182, http://www.isprambiente.gov.it/Media/carg/note_illustrative/182_Guastalla.pdf, Table 1, pp. 25-26.

Sheet 187, http://www.isprambiente.gov.it/Media/carg/note_illustrative/187_Codigoro.pdf, Table 1, p. 82.

Sheet 201, http://www.isprambiente.gov.it/Media/carg/note_illustrative/201_Modena.pdf, Table 1, p. 23.

Sheet 202, http://www.isprambiente.gov.it/Media/carg/note_illustrative/202_Giovanni_Persiceto.pdf, Table 1, p. 27.

Sheet 203, http://www.isprambiente.gov.it/Media/carg/note_illustrative/203_Poggiorenatico.pdf, Table 3, p. 24.

Sheet 204, http://www.isprambiente.gov.it/Media/carg/note_illustrative/204_Portomaggiore.pdf, Table 2, p. 22.

Sheet 205, http://www.isprambiente.gov.it/Media/carg/note_illustrative/205_Comacchio.pdf, Table 3, p. 43.

Sheet 221, http://www.isprambiente.gov.it/Media/carg/note_illustrative/221_Bologna.pdf, Table 3, pp. 45-46.

Sheet 222, http://www.isprambiente.gov.it/Media/carg/note_illustrative/222_Lugo.pdf, Table 2, p. 25.

Sheet 223, http://www.isprambiente.gov.it/Media/carg/note_illustrative/223_Ravenna.pdf, Table 1, p. 50.

Sheet 239, http://www.isprambiente.gov.it/Media/carg/note_illustrative/239_Faenza.pdf, Table 3, p. 46.

Sheets 240-241, http://www.isprambiente.gov.it/Media/carg/note_illustrative/240_241_ForliCervia.pdf, Table 4, p. 43.

Sheet 256, http://www.isprambiente.gov.it/Media/carg/note_illustrative/256_Rimini.pdf, Table 3, p. 72.

Sheet 268, the original data is available at https://applicazioni.regione.emilia-romagna.it/cartografia_sgss/user/viewer.jsp?service=geologia.

Acknowledgements

We are grateful to the Regione Emilia-Romagna Geological Survey for the full access to the database and for the recovery of core S1.

Author contribution

BC: lead author, research design, sampling campaign, geological interpretation; LB: second author, sampling campaign, geological interpretation; AA: principal investigator.

Appendix. Supplementary data

Table 1 – List of radiocarbon dates. GMI: Geological Map of Italy (see Data Availability). Proj.: projected. Frag.: fragment.

Core	Sample depth (m)	Sample code	^{14}C age	Cal year BP (2σ range)	Cal year BP (mean value)	Material	Source	Figure
187 S1	7.95	KGM-TCa180071	1860±30	1360-1180	1270±90	Shell	Amorosi et al., 2019	6a, 7c
	15.90	KGM-TCa180072	2340±30	1900-1690	1800±100	Shell	Amorosi et al., 2019	6a, 7c
	19.75	KGM-TWd180579	2570±20	2180-1950	2070±110	Wood	Amorosi et al., 2019	6a, 7c
	25.85	Beta Analytic-187 S1_25.85	8250±60	9420-9070	9230±170	Plant frag.	GMI, Sheet 187	6a, 7c
	50.05	Beta Analytic-187 S1_50.05	41750±1000	-	45700±1900	Peat	GMI, Sheet 187	6a, 7c
EM 7	5.60	KGM-OWd150653	2340±40	2490-2305	2400±90	Wood	Amorosi et al., 2017a	6a
	19.35	KGM-OCa150088	2910±40	2865-2530	2790±170	Plant frag.	Amorosi et al., 2017a	6a
	21.30	KGM-OCa160023	6430±40	6880-6620	6750±130	Shell	Amorosi et al., 2017a	6a
	22.40	KGM-OWd150654	7540±50	8450-8200	8355±120	Plant frag.	Amorosi et al., 2017a	6a
	26.70	KGM-OWd150655	8010±50	9050-8650	8860±200	Wood	Amorosi et al., 2017a	6a
205 S10	5.50	KGM-OWd170607	970±30	720-560	660±80	Plant frag.	Amorosi et al., 2019	6a, 6b
	21.75	KGM-OCa170052	3750±40	3640-3380	3510±130	Shell frag.	Amorosi et al., 2019	6a, 6b
	25.10	UCIAMS-51672	4960±15	5255-4985	5120±130	Shell	(Scarponi et al., 2013)	6a, 6b
	29.80	KGM-OWd170610	8010±50	8700-8420	8560±140	Plant frag.	This paper	6a, 6b
205 S4	34.40	ENEA-205 S4_34.4	15280 ± 380	19455–17700	18545±880	Organic clay	(Amorosi et al., 2003)	6a, 6b (Proj. 205S10)
205 S14	31.70	Beta analytic - 205 S14_31.7	10,480 ± 40	12570–12375	12430±100	Organic clay	Amorosi et al., 2003	6a, 6b (Proj. 205S10)

223 S17	23.60	ETH-50473	4400±35	4505-4230	4365±140	Shell	Campo et al., 2017	6a, 7b
223 S1	16.10	LODYC-223 S17_16.1	3305±60	3645-3395	3535±120	Organic clay	(Amorosi et al., 1999b)	6a, 7a (Proj.223P461)
	25.6	LODYC-223 S17_25.6	8170±50	9270-9010	9130±130	Wood	Amorosi et al., 1999b	6a, 7a (Proj.223P461)
	32.8	LLNL-CAMS-223 S17_32.8	25580±170	30315-29260	29755±530	Organic clay	Amorosi et al., 1999b	6a, 7a (Proj.223P461)
	45.00	LLNL-CAMS-223 S17_45	33530±440	38855-36550	37758±1150	Wood	Amorosi et al., 1999b	6a, 7a (Proj.223P461)
240 S6	21.55	CEDAD - LTL13434A	7384±45	8037-7856	7958±90	Mollusk shell	Campo et al., 2017	6a
	38.80	KGM-OCa160036	26070±150	30780-29830	30350±480	Organic clay	This paper	6a
240 S8	21.0	Beta analytic - 240 S8_21	8840±100	10195-9600	9915±300	Organic clay	GMI, Sheets 240-241	6a
	30.5	Beta analytic - 240 S8_30.5	13270±50	16145-15755	15955±200	Organic clay	GMI, Sheets 240-241	6a
Cervia	16.45	KGM-OCa150092	6720±40	7665-7555	7585±50	Organic clay	Campo et al., 2017	6a
241 S1	10.1	LLNL-CAMS-241 S1_10.1	5840±50	6755-6500	6645±130	Organic clay	GMI, Sheets 240-241	6a
	14.9	LLNL-CAMS-241 S1_14.9	9520±50	10905-10655	10875±120	Organic clay	GMI, Sheets 240-241	6a
	23.7	LLNL-CAMS-241 S1_23.7	14290±60	17610-17175	17400±220	Organic clay	GMI, Sheets 240-241	6a
	39.8	LLNL-CAMS-241 S1_39.8	38390±560	43320-41745	42520±790	Organic clay	GMI, Sheets 240-241	6a
256 S6	19.9	LLNL-CAMS-256 S6_19.9	9730±50	11245-11075	11145±90	Organic clay	GMI, Sheet 256	6a
	32.0	ETH-256 S6_32	29780±320	34545-33375	33925±580	Organic clay	GMI, Sheet 256	6a
	38.0	ETH-256 S6_38	33140±410	38445-36320	37370±1050	Wood	GMI, Sheet 256	6a
256 S3	6.6	ETH-256 S3_6.6	4040±70	4830-4400	4560±220	Organic clay	GMI, Sheet 256	6a
	13.9	ETH-256 S3_13.9	11950±85	14030-13560	13800±230	Wood	GMI, Sheet 256	6a
	15.4	ETH-256 S3_15.4	21590±210	26290-25470	25870±410	Wood	GMI, Sheet 256	6a
	26.3	ETH-256 S3_26.3	36800±710	42480-40050	41310±1200	Wood	GMI, Sheet 256	6a
256 110 P505	14.5	ENEA-256P505_14.5	12710±150	15650-14370	15060±640	Organic clay	GMI, Sheet 256	6a
256 160 P507	7.0	LODYC-256160P507_7	5335±60	6280-5980	6110±150	Wood	GMI, Sheet 256	6a
268 010 A501	7.0	LODYC-268010A501_7	15385±220	19140-18120	18640±510	Organic clay	This work	6a (Proj.268 S2)
205 S2	6.05	KGM-OCa160037	4610±40	4805-4515	4660±140	Shell	Amorosi et al., 2019	6b
	10.95	KGM-OCa170048	4480±40	4875-4640	4795±120	Shell	Amorosi et al., 2019	6b
	16.00	KGM-OCa160038	7000±50	7480-7255	7370±110	Shell	Amorosi et al., 2019	6b

	16.70	KGM-OCa170049	7910±50	8570-8380	8470±90	Shell	Amorosi et al., 2019	6b
	18.95	KGM-OWd170603-1	10960±40	12710-12570	12640±70	Plant frag.	Amorosi et al., 2019	6b
	19.30	KGM-OWd170604	7780±40	8430-8220	8350±100	Plant frag.	Amorosi et al., 2019	6b
	20.50	ENEA-205 S2_20.50	8400±100	9545-9130	9375±200	Organic clay	GMI, Sheet 205	6b
	21.15	KGM-OWd170605	7970±40	9000-8650	8840±180	Plant frag.	Amorosi et al., 2019	6b
205 S1	9.80	ETH-205 S1_9.80	7535±70	8450-8185	8335±130	Shell	Amorosi et al., 2003	6b
	14.80	ENEA-205 S1_14.80	25300±180	29860-28870	29365±500	Organic clay	Amorosi et al., 2003	6b
	24.50	ENEA-205 S1_24.50	30150±520	35260-33350	34260±950	Organic clay	Amorosi et al., 2003	6b
B1	15.1	KGM-TSa180029a	21690±80	26110-25780	25950±160	Organic clay	This paper	6b
	17.7	KGM-TSa180033a	37590±260	42390-41570	41980±410	Organic clay	This paper	6b
204 S3	4.25	KGM-TWd180291	5520±40	6175-5935	6050±120	Plant frag.	Amorosi et al., 2019	6b
B4	6.05	KGM-TWd190156	2770±30	2950-2780	2860±80	Peat	This paper	7c
	8.4	KGM-TWd190159	4180±30	4770-4610	4720±80	Wood	This paper	6b
	12.4	KGM-TWd190165	6470±30	7440-7320	7380±60	Wood	This paper	6b, 7c
	15.6	KGM-TSa190029	9780±60	11320-11080	11200±120	Organic clay	This paper	6b, 7c
	21.3	KGM-TWd190167	22710±90	27350-26690	27080±330	Peat	This paper	6b, 7c
	24.96	KGM-TSa190030a	28660±210	33420-31920	32740±750	Organic clay	This paper	6b, 7c
	30.85	KGM-TSa190031	40130±450	44620-42980	43760±820	Organic clay	This paper	6b, 7c
204 S4	5.8	Beta analytic - 204 S4_5.8	1780±60	1830-1560	1690±130	Peat	GMI, Sheet 204	6b
	9.35	Beta analytic - 204 S4_9.35	5280±50	6190-5930	6060±130	Peat	GMI, Sheet 204	6b
	21.0	ENEA-204 S4_26.8	35500±3000	48350-35090	41030±6600	Organic clay	GMI, Sheet 204	6b
203 S9	11.45	ENEA-203 S9_11.45	4350±80	5290-4810	4980±240	Organic clay	GMI, Sheet 203	6b, 8a
	20.25	ENEA-203 S9_20.25	13450±320	17170-15270	16230±950	Organic clay	GMI, Sheet 203	6b
202 S1	11.40	Beta analytic - 202 S1_11.4	9360±40	10700-10490	10600±100	Organic clay	GMI, Sheet 202	6b
202 S12	7.9	Beta analytic - 202 S12_7.9	1480±80	1544-1275	1410±130	Peat	GMI, Sheet 202	6b
	15.0	ENEA-202 S12_15.0	8020±90	9130-8600	8860±260	Pedoge-nized clay	GMI, Sheet 202	6b

PP	31.30	CIRCE – PP 31.3	>45000	-	-	Organic clay	Amorosi et al., 2017b	6b
SFP	11.7	KGM-OWd160291	2480±40	2730-2370	2570±180	Wood	This work	6b
	35.05	CIRCE – DSH6715_H	42400±800	47600-44370	45870±1600	Pedoge-nized clay	This work	6b
Med	38.4	CIRCE – Med_38.4	>45000	-	-	Organic clay	This work	6b, 8b
SP	9.60	KGM-OSn160003	4360±40	5040-4840	4930±100	Organic clay	This work	6b
Conc	13.6	KGM-OSn160002	12230±70	14510-13900	14160±300	Pedoge-nized clay	This work	6b
EM 19	10.5	KGM-OWd160292	23080±140	27640-27120	27900±260	Wood	This work	6b
Mn S1	18.8	ENEA-Mn S1_18.8	38600±1050	44750-41270	42900±1700	Organic clay	Amorosi et al., 2008	6b, 8c
	27.7	ENEA-Mn S1_27.7	>45000	-	-	Organic clay	Amorosi et al., 2008	6b, 8c
239 S4	14.0	ETH-239 S4_14	6255±75	7330-6950	7160±190	Charcoal	GMI, Sheet 239	7a
	28.0	ETH-239 S4_28	12920±100	15770-15140	15450±310	Peat	GMI, Sheet 239	7a
239 S6	13.0	Beta Analytic-239 S6_13	11840±150	14060-13390	13690±330	Charcoal	GMI, Sheet 239	7a, 7c (Proj.222 S10)
223 S11	6.25	LODYC-223 S11_6.25	1235±40	1270-1060	1170±100	Peat	GMI, Sheet 223	7b (Proj.)
222 S2	7.0	Beta Analytic-222 S2_7.0	340±60	510-290	390±110	Peat	GMI, Sheet 222	7b
	17.0	Beta Analytic-222 S2_17.0	6000±60	6990-6670	6840±160	Peat	GMI, Sheet 222	7b
	20.9	Beta Analytic-222 S2_20.9	7420±60	8380-8150	8250±110	Organic clay	GMI, Sheet 222	7b
	26.2	Beta Analytic-222 S2_26.2	19770±150	24190-23420	23800±380	Peat	GMI, Sheet 222	7b
221 S1	16.35	LODYC-221 S1_16.35	8945±200	10550-9540	10030±500	Organic clay	GMI, Sheet 221	7b
	29.8	LODYC-221 S1_29.8	21780±800	27700-24410	26130±1600	Organic clay	GMI, Sheet 221	7b
EM 8	5.45	OWd160064	4890±50	5740-5480	5630±130	Peat	(Bruno et al., 2017)	7c
	7.30	OWd160065	5800±400	6720-6490	6600±110	Wood	(Bruno et al., 2017)	7c
	22.40	OWd160066	7950±40	8890-8640	8820±120	Wood	(Bruno et al., 2017)	7c
B3	3.55	KGM-TWd190145	2120±20	2160-2000	2090±80	Peat	This paper	7c
	8.5	KGM-TWd190152	6480±30	7440-7310	7380±60	Peat	This paper	7c
	9.2	KGM-TSa190025	8870±50	10180-9760	10000±210	Bulk sediment	This paper	7c
	12.6	KGM-TSa190026	23750±140	28130-27580	27820±270	Bulk sediment	This paper	7c
	15.6	KGM-TSa190028	28590±200	33300-31840	32630±730	Organic clay	This paper	7c

204 S17	12.8	KGM-OWd170597-1	3850±30	4410-4150	4270±130	Plant frag.	This paper	7c
	17.0	KGM-OWd170601-1	6840±30	7740-7600	7670±70	Plant frag.	This paper	7c
B2	11.15	KGM-TWd180570a	650±30	610-550	610±30	Wood	This paper	7c
	16.6	KGM-TWd180575a	2730±30	2880-2760	2820±60	Wood	This paper	7c
	20.25	KGM-TWd180577a	5390±30	6290-6170	6210±60	Wood	This paper	7c
	22.05	KGM-TSa180035a	9500±40	10870-10650	10840±100	Bulk sediment	This paper	7c
	29.8	KGM-TSa180036a	246300±90	28900-28410	28660±240	Bulk sediment	This paper	7c
222 S17	5.0	LODYC-222 S17_5	2635±80	2950-2480	2730±230	Organic clay	GMI, Sheet 222	7b (Proj.), 7c
222 S6	3.9	Beta Analytic-222 S6_3.9	2100±70	2210-1900	2090±150	Organic clay	GMI, Sheet 222	7c
	18.8	Beta Analytic-222 S6_18.8	11560±60	13500-13270	13390±110	Organic clay	GMI, Sheet 222	7b (Proj.), 7c
	26.8	Beta Analytic-222 S6_26.8	18000±150	22260-21400	21810±430	Peat	GMI, Sheet 222	7b (Proj.), 7c
222 S10	12.5	Beta Analytic-222 S10_12.5	14280±140	17800-16980	17380±410	Organic clay	GMI, Sheet 222	7c
	21.2	Beta Analytic-222 S10_21.2	32550±600	36770-35350	36770±700	Peat	GMI, Sheet 222	7c
	35.5	Beta Analytic-222 S10_35.5	>44500	-	-	Wood	GMI, Sheet 222	7c
221 S5	24.0	LODYC – 221 S5_24	19760±900	26010-21930	23970±2000	Organic clay	GMI, Sheet 221	8a
221 S3	15.20	LODYC – 221 S3_15.2	13025±160	16070-15150	15610±460	Organic clay	GMI, Sheet 221	8a
	22.80	LODYC – 221 S3_22.8	>35000	-	-	Organic clay	GMI, Sheet 221	8a
CS	23.05	ETH-50655	26917±89	31190-30820	31010±180	Shell	This work	8b (Proj.)
201 S6	17.6	ENEA-201 S6_17.6	4530±60	5330-4970	5170±180	-	GMI, Sheet 201	8b
	33.9	ENEA-201 S6_33.9	26500±200	31080-30370	30750±350	-	GMI, Sheet 201	8b
201 S4	9.9	ENEA-201 S4_9.9	7780±110	8810-8380	8620±210	-	GMI, Sheet 201	8b
	15.7	ENEA-201 S4_15.7	12200±180	14990-13710	14240±640	-	GMI, Sheet 201	8b
	21.4	ENEA-201 S4_21.4	19340±200	23840-22800	23300±520	-	GMI, Sheet 201	8b
	24.1	ENEA-201 S4_24.1	21250±350	26190-24600	25510±800	-	GMI, Sheet 201	8b
201 S3	17.15	ENEA-201 S3_17.15	6890±80	7870-7580	7740±140	-	GMI, Sheet 201	8b
	28.7	ENEA-201 S3_28.7	14000±100	17360-16620	16990±370	-	GMI, Sheet 201	8b
182 S10	6.4	ENEA-182 S10_6.4	2890±50	3170-2870	3030±150	Organic clay	GMI, Sheet 182	8c
	30.5	ENEA-182 S10_30.5	47900±550	49090-46860	47960±1100	Organic clay	GMI, Sheet 182	8c
182 S15	10.3	ENEA-182 S15_10.5	4930±80	5895-5485	5680±200	Organic clay	(Pavesi, 2009)	8c

	19.5	ENEA-182 S15_19.5	15450±130	18967-18429	18715±270	Wood	Pavesi, 2009	8c
	34.7	ENEA-182 S15_34.7	27300±600	32961-30371	31380±1300	Wood	Pavesi, 2009	8c
	45.0	ENEA-182 S15_45.0	>45000	-	-	Organic clay	Pavesi, 2009	8c
182 S3	3.65	ENEA-182 S3_3.65	1830±60	1900-1600	1760±150	Soil	GMI, Sheet 182	8c
	14.1	ENEA-182 S3_14.1	15750±110	19310-18760	19020±270	Soil	GMI, Sheet 182	8c
	18.4	ENEA-182 S3_18.4	17850±150	22020-21140	21610±440	Soil	GMI, Sheet 182	8c

References

Aitken, M.J., 1985. Thermoluminescence dating. Academic Press, London.

Amadori, C., Toscani, G., Di Giulio, A., Maesano, F.E., D'Ambrogi, C., Ghielmi, M., Fantoni, R., 2019. From cylindrical to non-cylindrical foreland basin: Pliocene–Pleistocene evolution of the Po Plain–Northern Adriatic basin (Italy). Basin Res. 991–1015. https://doi.org/10.1111/bre.12369

Amorosi, A., Antonioli, F., Bertini, A., Marabini, S., Mastronuzzi, G., Montagna, P., Negri, A., Rossi, V., Scarponi, D., Taviani, M., Angeletti, L., Piva, A., Vai, G.B., 2014. The Middle-Upper Pleistocene Fronte Section (Taranto, Italy): An exceptionally preserved marine record of the Last Interglacial. Glob. Planet. Change 119, 23–38. https://doi.org/10.1016/j.gloplacha.2014.04.007

Amorosi, A., Bruno, L., Campo, B., Costagli, B., Dinelli, E., Hong, W., Sammartino, I., Vaiani, S.C., 2019. Tracing clinothem geometry and sediment pathways in the prograding Holocene Po Delta system through integrated core stratigraphy. Basin Res. 1–10. https://doi.org/10.1111/bre.12360

Amorosi, A., Bruno, L., Campo, B., Morelli, A., 2015. The value of pocket penetration tests for the high-resolution palaeosol stratigraphy of late Quaternary deposits. Geol. J. 50, 670–682.

Amorosi, A., Bruno, L., Campo, B., Morelli, A., Rossi, V., Scarponi, D., Hong, W., Bohacs, K.M., Drexler, T.M., 2017a. Global sea-level control on local parasequence architecture from the Holocene record of the Po Plain, Italy. Mar. Pet. Geol. 87, 99–111. https://doi.org/10.1016/j.marpetgeo.2017.01.020

Amorosi, A., Bruno, L., Cleveland, D.M., Morelli, A., Hong, W., 2017b. Paleosols and associated channel-belt sand bodies from a continuously subsiding late quaternary system (Po basin, Italy): New insights into continental sequence stratigraphy. Bull. Geol. Soc. Am. 129, 449–463. https://doi.org/10.1130/B31575.1

Amorosi, A., Centineo, M.C., Colalongo, M.L., Pasini, G., Sarti, G., Vaiani, S.C., 2003. Facies architecture and latest Pleistocene–Holocene depositional history of the Po Delta (Comacchio area), Italy. J. Geol. 111, 39–56.

Amorosi, A., Colalongo, M.L., 2005. The linkage between alluvial and coeval nearshore marine successions: evidence from the Late Quaternary record of the Po River Plain, Italy. Fluv. Sedimentol. VII 255–275.

Amorosi, A., Colalongo, M.L., Fiorini, F., Fusco, F., Pasini, G., Vaiani, S.C., Sarti, G., 2004. Palaeogeographic and palaeoclimatic evolution of the Po Plain from 150-ky core records. Glob. Planet. Change 40, 55–78. https://doi.org/10.1016/S0921-8181(03)00098-5

Amorosi, A., Colalongo, M.L., Fusco, F., Pasini, G., Fiorini, F., 1999a. Glacio-eustatic control of continental-shallow marine cyclicity from late quaternary deposits of the southeastern Po Plain, northern Italy. Quat. Res. 52, 1–13. https://doi.org/10.1006/qres.1999.2049

Amorosi, A, Colalongo, M., Pasini, G., Preti, D., 1999b. Sedimentary response to Late Quaternary sea-level changes in the Romagna coastal plain(northern Italy). Sedimentology 46, 99–121.

Amorosi, A., Forlani, L., Fusco, F., Severi, P., 2001. Cyclic patterns of facies and pollen associations from late quaternary deposits in the subsurface of Bologna. GeoActa 1, 83–94.

Amorosi, A., Marchi, N., 1999. High-resolution sequence stratigraphy from piezocone tests: An example from the Late Quaternary deposits of the southeastern Po Plain. Sediment. Geol. 128, 67–81. https://doi.org/10.1016/S0037-0738(99)00062-7

Amorosi, A., Pavesi, M., Ricci Lucchi, M., Sarti, G., Piccin, A., 2008. Climatic signature of cyclic fluvial architecture from the Quaternary of the central Po Plain, Italy. Sediment. Geol. 209, 58–68. https://doi.org/10.1016/j.sedgeo.2008.06.010

Antonioli, F., 2012. Sea level change in Western-Central Mediterranean since 300 kyr: Comparing global sea level curves with observed data. Alp. Mediterr. Quat. 25, 15–23.

Antonioli, F., Anzidei, M., Amorosi, A., Lo Presti, V., Mastronuzzi, G., Deiana, G., De Falco, G., Fontana, A., Fontolan, G., Lisco, S., Marsico, A., Moretti, M., Orrù, P.E., Sannino, G.M., Serpelloni, E., Vecchio, A., 2017. Sea-level rise and potential drowning of the Italian coastal plains: Flooding risk scenarios for 2100. Quat. Sci. Rev. 158, 29–43. https://doi.org/10.1016/j.quascirev.2016.12.021

Antonioli, F., Bard, E., Potter, E.K., Silenzi, S., Improta, S., 2004. 215-ka history of sea-level oscillations from marine and continental layers in Argentarola Cave speleothems (Italy). Glob. Planet. Change 43, 57–78. https://doi.org/10.1016/j.gloplacha.2004.02.004

Banerjee, D., Murray, A.S., Bøtter-Jensen, L., Lang, A., 2001. Equivalent dose estimation using a single aliquot of polymineral fine grains. Radiat. Meas. 33, 73–94.

Bard, E., Antonioli, F., Silenzi, S., 2002. Sea-level during the penultimate interglacial period based on a submerged stalagmite from Argentarola Cave (Italy). Earth Planet. Sci. Lett. 196, 135–146. https://doi.org/10.1016/S0012-821X(01)00600-8

Bard, E., Hamelin, B., Fairbanks, R.G., 1990. U-Th ages obtained by mass spectrometry in corals from Barbados: Sea level during the past 130,000 years. Nature 346, 456–458. https://doi.org/10.1038/346456a0

Bardají, T., Goy, J.L., Zazo, C., Hillaire-Marcel, C., Dabrio, C.J., Cabero, A., Ghaleb, B., Silva, P.G., Lario, J., 2009. Sea level and climate changes during OIS 5e in the Western Mediterranean. Geomorphology 104, 22–37. https://doi.org/10.1016/j.geomorph.2008.05.027

Basili, R., Barba, S., 2007. Migration and shortening rates in the northern Apennines, Italy: Implications for seismic hazard. Terra Nov. 19, 462–468. https://doi.org/10.1111/j.1365-3121.2007.00772.x

Blum, M.D., Martin, J., Milliken, K., Garvin, M., 2013. Paleovalley systems: Insights from Quaternary analogs and experiments. Earth-Science Rev. 116, 128–169. https://doi.org/10.1016/j.earscirev.2012.09.003

Blum, M.D., Aslan, A., 2006. Signatures of climate vs. sea-level change within incised valley-fill successions: Quaternary examples from the Texas GULF Coast. Sediment. Geol. 190, 177–211. https://doi.org/10.1016/j.sedgeo.2006.05.024

Blum, M.D., Törnqvist, T.E., 2000. Fluvial responses to climate and sea-level change: A review and look forward. Sedimentology 47, 2–48. https://doi.org/10.1046/j.1365-3091.2000.00008.x

Boccaletti, M., Corti, G., Martelli, L., 2011. Recent and active tectonics of the external zone of the Northern Apennines (Italy). Int. J. Earth Sci. 100, 1331–1348. https://doi.org/10.1007/s00531-010-0545-y

Bondesan, M., Cibin, U., Colalongo, M., Pugliese, N., Stefani, M., Tsakiridis, E., Vaiani, S.C., Vincenzi, S., 2006. Benthic communities and sedimentary facies recording late Quaternary environmental fluctuations in a Po Delta subsurface succession (Northern Italy), in: 2nd and 3rd Italian Meeting on

Environmental Micropaleontology. Grzybowski Founfation Special Publication, pp. 21–31.

Bordoni, P., Valensise, G., 1998. Deformation of the 125 ka marine terrace in Italy: tectonic implications. Geol. Soc. Spec. Publ. 146, 71–110. https://doi.org/10.1144/GSL.SP.1999.146.01.05

Bøtter-Jensen, L., 1997. Luminescence techniques: instrumentation and methods. Radiat. Meas. 27, 749–768.

Bøtter-Jensen, L., 1988. The automated Risø TL dating reader system. Int. J. Radiat. Appl. Instrumentation. Part D. Nucl. Tracks Radiat. Meas. 14, 177–180.

Bøtter-Jensen, L., Bulur, E., Duller, G.A.T., Murray, A.S., 2000. Advances in luminescence instrument systems. Radiat. Meas. 32, 523–528.

Bruno, L., Bohacs, K.M., Campo, B., Drexler, T.M., Rossi, V., Sammartino, I., Scarponi, D., Hong, W., Amorosi, A., 2017. Early Holocene transgressive palaeogeography in the Po coastal plain (northern Italy). Sedimentology 64, 1792–1816. https://doi.org/10.1111/sed.12374

Burrato, P., Ciucci, F., Valensise, G., 2003. An inventory of river anomalies in the Po Plain, Northern Italy: Evidence for active blind thrust faulting. Ann. Geophys. 46, 865–882. https://doi.org/10.4401/ag-3459

Busschers, F.S., Kasse, C., van Balen, R.T., Vandenberghe, J., Cohen, K.M., Weerts, H.J.T., Wallinga, J., Johns, C., Cleveringa, P., Bunnik, F.P.M., 2007. Late Pleistocene evolution of the Rhine-Meuse system in the southern North Sea basin: imprints of climate change, sea-level oscillation and glacio-isostacy. Quat. Sci. Rev. 26, 3216–3248. https://doi.org/10.1016/j.quascirev.2007.07.013

Busschers, F.S., Weerts, H.J.T., Wallinga, J., Cleveringa, P., Kasse, C., de Wolf, H., Cohen, K.M., 2005. Sedimentary architecture and optical dating of Middle and Late Pleistocene Rhine-Meuse deposits - Fluvial response to climate change, sea-level fluctuation and glaciation. Geol. en Mijnbouw/Netherlands J. Geosci. 84, 25–41. https://doi.org/10.1017/s0016774600022885

Campo, B., Amorosi, A., Bohacs, K.M., in press. Late Quaternary sequence stratigraphy as a tool for groundwater exploration: lessons from the Po River Basin (northern Italy). Am. Assoc. Pet. Geol. Bull. https://doi.org/10.1306/06121918116

Campo, B., Amorosi, A., Bruno, L., 2016. Contrasting alluvial architecture of Late Pleistocene and Holocene deposits along a 120-km transect from the central Po Plain (northern Italy). Sediment. Geol. 341, 265–275.

Campo, B., Amorosi, A., Vaiani, S.C., 2017. Sequence stratigraphy and late Quaternary paleoenvironmental evolution of the Northern Adriatic coastal plain (Italy). Palaeogeogr. Palaeoclimatol. Palaeoecol. 466, 265–278. https://doi.org/10.1016/j.palaeo.2016.11.016

Caputo, R., Pellegrinelli, A., Bignami, C., Bondesan, A., Mantovani, A., Stramondo, S., Russo, P., 2015. High-precision levelling, DInSAR and geomorphological effects in the Emilia 2012 epicentral area. Geomorphology 235, 106–117. https://doi.org/10.1016/j.geomorph.2015.02.002

Carboni, M.G., Bergamin, L., Di Bella, L., Esu, D., Cerone, E.P., Antonioli, F., Verrubbi, V., 2010. Palaeoenvironmental reconstruction of late Quaternary foraminifera and molluscs from the ENEA borehole (Versilian plain, Tuscany, Italy). Quat. Res. 74, 265–276. https://doi.org/10.1016/j.yqres.2010.07.006

Carminati, E., Di Donato, G., 1999. Separating natural and anthropogenic vertical movements in fast subsiding areas: The Po plain (N. Italy) case. Geophys. Res. Lett. 26, 2291–2294. https://doi.org/10.1029/1999GL900518

Carminati, E., Doglioni, C., 2012. Alps vs. Apennines: The paradigm of a tectonically asymmetric Earth. Earth-Science Rev. 112, 67–96. https://doi.org/10.1016/j.earscirev.2012.02.004

Carminati, E., Doglioni, C., Scrocca, D., 2003. Apennines subduction-related subsidence of Venice (Italy). Geophys. Res. Lett. 30, 1–4. https://doi.org/10.1029/2003GL017001

Carr, A.S., Bateman, M.D., Roberts, D.L., Murray-Wallace, C. V., Jacobs, Z., Holmes, P.J., 2010. The last interglacial sea-level high stand on the southern Cape coastline of South Afri~ Quat. Res. 73, 351–363. https://doi.org/10.1016/j.yqres.2009.08.006

Castorina, F., Vaiani, S.C., 2018. Riverine influence in Sr isotope ratio of mollusk shells and relationship with foraminiferal assemblages in a late Quaternary succession of the Po River Delta (northern Italy). Ital. J. Geosci. 137, 31–37. https://doi.org/10.3301/IJG.2017.15

Chappell, J., Omura, A., Esat, T., McCulloch, M., Pandolfi, J., Ota, Y., Pillans, B., 1996. Reconciliation of late Quaternary sea levels derived from coral terraces at Huon Peninsula with deep sea oxygen isotope records. Earth Planet. Sci. Lett. 141, 227–236. https://doi.org/10.1016/0012-821x(96)00062-3

Chappell, J., Shackleton, N., 1986. Oxygen isotopes and sea level. Nature 324, 137–140.

Church, J.A., Clark, P.U., Cazenave, A., Gregory, J.M., Jevrejeva, S., Levermann, A., Merrifield, M.A., Milne, G.A., Nerem, R.S., Nunn, P.D., 2013. Sea level change. PM Cambridge University Press.

Clark, P.U., Huybers, P., 2009. Global change: Interglacial and future sea level. Nature 462, 856–857. https://doi.org/10.1038/462856a

Creveling, J.R., Mitrovica, J.X., Hay, C.C., Austermann, J., Kopp, R.E., 2015. Revisiting tectonic corrections applied to Pleistocene sea-level highstands. Quat. Sci. Rev. 111, 72–80. https://doi.org/10.1016/j.quascirev.2015.01.003

De Santis, V., Caldara, M., de Torres, T., Ortiz, J.E., 2010. Stratigraphic units of the Apulian Tavoliere plain (Southern Italy): Chronology, correlation with marine isotope stages and implications regarding vertical movements. Sediment. Geol. 228, 255–270. https://doi.org/10.1016/j.sedgeo.2010.05.001

Durcan, J.A., King, G.E., Duller, G.A.T., 2015. DRAC: Dose Rate and Age Calculator for trapped charge dating. Quat. Geochronol. 28, 54–61.

Dutton, A., Carlson, A.E., Long, Aj., Milne, G.A., Clark, P.U., DeConto, R., Horton, B.P., Rahmstorf, S., Raymo, M.E., 2015. Sea-level rise due to polar ice-sheet mass loss during past warm periods. Science (80-.). 349, aaa4019.

Dutton, A., Lambeck, K., 2012. Ice volume and sea level during the last interglacial. Science (80-.). 337, 216–219. https://doi.org/10.1126/science.1205749

Ferranti, L., Antonioli, F., Anzidei, M., Monaco, C., Stocchi, P., 2010. The timescale and spatial extent of vertical tectonic motions in Italy: Insights from coastal tectonic studies. Rend. Online Soc. Geol. Ital. 11, 683–684. https://doi.org/10.3809/jvirtex.2009.00255

Ferranti, L., Antonioli, F., Mauz, B., Amorosi, A., Dai Pra, G., Mastronuzzi, G., Monaco, C., Orrù, P., Pappalardo, M., Radtke, U., Renda, P., Romano, P., Sansò, P., Verrubbi, V., 2006. Markers of the last interglacial sea-level high stand along the coast of Italy: Tectonic implications. Quat. Int. 145–146, 30–54. https://doi.org/10.1016/j.quaint.2005.07.009

Fiorini, F., 2004. Benthic foraminiferal associations from Upper Quaternary deposits of southeastern Po Plain, Italy. Micropaleontology 50, 45–58. https://doi.org/10.2113/50.1.45

Fontana, A., Mozzi, P., Bondesan, A., 2010. Late Pleistocene evolution of the Venetian-Friulian Plain. Rend. Lincei 21, 181–196. https://doi.org/10.1007/s12210-010-0093-1

Fontana, A., Mozzi, P., Marchetti, M., 2014. Alluvial fans and megafans along the southern side of the Alps.

Sediment. Geol. 301, 150–171. https://doi.org/10.1016/j.sedgeo.2013.09.003
Galili, E., Zviely, D., Ronen, A., Mienis, H.K., 2007. Beach deposits of MIS 5e high sea stand as indicators for tectonic stability of the Carmel coastal plain, Israel. Quat. Sci. Rev. 26, 2544–2557. https://doi.org/10.1016/j.quascirev.2007.06.027
Ghielmi, M., Minervini, M., Nini, C., Rogledi, S., Rossi, M., 2013. Late Miocene-Middle Pleistocene sequences in the Po Plain - Northern Adriatic Sea (Italy): The stratigraphic record of modification phases affecting a complex foreland basin. Mar. Pet. Geol. 42, 50–81. https://doi.org/10.1016/j.marpetgeo.2012.11.007
Guérin, G., Mercier, N., Adamiec, G., 2011. Dose-rate conversion factors: update. Anc. TL 29, 5–8.
Guillaume, M.M.M., Reyss, J.L., Pirazzoli, P.A., Bruggemann, J.H., 2013. Tectonic stability since the last interglacial offsets the Glorieuses Islands from the nearby Comoros archipelago. Coral Reefs 32, 719–726. https://doi.org/10.1007/s00338-012-1006-9
Hori, K., Saito, Y., Zhao, Q., Wang, P., 2002. Evolution of the coastal depositional systems of the Changjiang (Yangtze) River in response to Late Pleistocene-Holocene sea-level changes. J. Sediment. Res. 72, 884–897. https://doi.org/10.1306/052002720884
Horton, B.P., Kopp, R.E., Dutton, A., Shaw, T.A., Carolina, N., 2019. Geological records of past sea-level changes as constraints for future projections. Past Glob. Chang. Mag. 27, 28–29. https://doi.org/10.22498/pages.27.1.28
Intergovernmental Panel on Climate Change, 2018. Global Warming of 1.5° C: An IPCC Special Report on the Impacts of Global Warming of 1.5° C Above Pre-industrial Levels and Related Global Greenhouse Gas Emission Pathways, in the Context of Strengthening the Global Response to the Threat of Climate Chang. Intergovernmental Panel on Climate Change.
Intergovernmental Panel on Climate Change, 2007. The physical science basis. Contrib. Work. Gr. I to fourth Assess. Rep. Intergov. Panel Clim. Chang. 996.
Kopp, R.E., Simons, F.J., Mitrovica, J.X., Maloof, A.C., Oppenheimer, M., 2009. Probabilistic assessment of sea level during the last interglacial stage. Nature 462, 863–867. https://doi.org/10.1038/nature08686
Kukla, G.J., Bender, M.L., de Beaulieu, J.-L., Bond, G., Broecker, W.S., Cleveringa, P., Gavin, J.E., Herbert, T.D., Imbrie, J., Jouzel, J., 2002. Last interglacial climates. Quat. Res. 58, 2–13.

https://doi.org/10.4135/9781446247501.n2234

Lambeck, K., Antonioli, F., Purcell, A., Silenzi, S., 2004. Sea-level change along the Italian coast for the past 10,000 yr. Quat. Sci. Rev. 23, 1567–1598. https://doi.org/10.1016/j.quascirev.2004.02.009

Maesano, F.E., D'Ambrogi, C., Burrato, P., Toscani, G., 2015. Slip-rates of blind thrusts in slow deforming areas: Examples from the Po Plain (Italy). Tectonophysics 643, 8–25. https://doi.org/10.1016/j.tecto.2014.12.007

Malinverno, A., Ryan, W.B.F., 1986. BBBn 5, 227–245.

Mariotti, G., Doglioni, C., 2000. The dip of the foreland monocline in the Alps and Apennines. Earth Planet. Sci. Lett. 181, 191–202. https://doi.org/10.1016/S0012-821X(00)00192-8

Martinson, D.G., Pisias, N.G., Hays, J.D., Imbrie, J., Moore, T.C., Shackleton, N.J., 1987. Age dating and the orbital theory of the ice ages: Development of a high-resolution 0 to 300,000-year chronostratigraphy. Quat. Res. 27, 1–29. https://doi.org/10.1016/0033-5894(87)90046-9

Matsu'ura, T., Komatsubara, J., Wu, C., 2019. Accurate determination of the Pleistocene uplift rate of the NE Japan forearc from the buried MIS 5e marine terrace shoreline angle. Quat. Sci. Rev. 212, 45–68. https://doi.org/10.1016/j.quascirev.2019.03.007

Mauz, B., Fanelli, F., Elmejdoub, N., Barbieri, R., 2012. Coastal response to climate change: Mediterranean shorelines during the Last Interglacial (MIS 5). Quat. Sci. Rev. 54, 89–98. https://doi.org/10.1016/j.quascirev.2012.02.021

Milli, S., D'Ambrogi, C., Bellotti, P., Calderoni, G., Carboni, M.G., Celant, A., Di Bella, L., Di Rita, F., Frezza, V., Magri, D., Pichezzi, R.M., Ricci, V., 2013. The transition from wave-dominated estuary to wave-dominated delta: The Late Quaternary stratigraphic architecture of Tiber River deltaic succession (Italy). Sediment. Geol. 284–285, 159–180. https://doi.org/10.1016/j.sedgeo.2012.12.003

Milli, S., Mancini, M., Moscatelli, M., Stigliano, F., Marini, M., Cavinato, G.P., 2016. From river to shelf, anatomy of a high-frequency depositional sequence: The Late Pleistocene to Holocene Tiber depositional sequence. Sedimentology 63, 1886–1928. https://doi.org/10.1111/sed.12277

Murray-Wallace, C. V., 2013. Eustatic Sea-Level Changes - Glacial-Interglacial Cycles, 2nd ed, Encyclopedia of Quaternary Science: Second Edition. Elsevier B.V. https://doi.org/10.1016/B978-0-444-53643-3.00132-1

Murray-Wallace, C. V., 2002. Pleistocene coastal stratigraphy, sea-level highstands and neotectonism of the southern Australian passive continental margin - A review. J. Quat. Sci. 17, 469–489. https://doi.org/10.1002/jqs.717

Murray-Wallace, C. V., Belperio, A.P., Dosseto, A., Nicholas, W.A., Mitchell, C., Bourman, R.P., Eggins, S.M., Grün, R., 2016. Last interglacial (MIS 5e) sea-level determined from a tectonically stable, far-field location, Eyre Peninsula, southern Australia. Aust. J. Earth Sci. 63, 611–630. https://doi.org/10.1080/08120099.2016.1229693

Murray-Wallace, C. V, Woodroffe, C.D., 2014. Quaternary sea-level changes: a global perspective. Cambridge University Press.

Murray, A.S., Wintle, A.G., 2000. Luminescence dating of quartz using an improved single-aliquot regenerative-dose protocol. Radiat. Meas. 32, 57–73.

Muttoni, G., Carcano, C., Garzanti, E., Ghielmi, M., Piccin, A., Pini, R., Rogledi, S., Sciunnach, D., 2003. Onset of major Pleistocene glaciations in the Alps. Geology 31, 989–992. https://doi.org/10.1130/G19445.1

Nakazawa, T., Sakata, K., Hongo, M., Nakazato, H., 2017. Transition from incised valley to barrier island systems during MIS 5e in the northern Chiba area, Kanto Plain, central Japan. Quat. Int. 456, 85–101. https://doi.org/10.1016/j.quaint.2017.06.031

Oliver, T.S.N., Kennedy, D.M., Tamura, T., Murray-Wallace, C. V., Konlechner, T.M., Augustinus, P.C., Woodroffe, C.D., 2018. Interglacial-glacial climatic signatures preserved in a regressive coastal barrier, southeastern Australia. Palaeogeogr. Palaeoclimatol. Palaeoecol. 501, 124–135. https://doi.org/10.1016/j.palaeo.2018.04.011

Ori, G.G., 1993. Continental depositional systems of the Quaternary of the Po Plain (northern Italy). Sediment. Geol. 83, 1–14.

Ori, G.G., Friend, P.F., 1984. Sedimentary basins formed and carried piggyback on active thrust sheets. Geology 12, 475–478. https://doi.org/10.1130/0091-7613(1984)12<475:SBFACP>2.0.CO;2

Otvos, E.G., 2015. The Last Interglacial Stage: Definitions and marine highstand, North America and Eurasia. Quat. Int. 383, 158–173. https://doi.org/10.1016/j.quaint.2014.05.010

Otvos, E.G., 2013. Rapid and widespread response of the Lower Mississippi River to eustatic forcing during the last glacial-interglacial cycle: Discussion. Bull. Geol. Soc. Am. 125, 1369–1374.

Otvos, E.G., 2005. Numerical chronology of Pleistocene coastal plain and valley development; extensive aggradation during glacial low sea-levels. Quat. Int. 135, 91–113. https://doi.org/10.1016/j.quaint.2004.10.026

Overpeck, J.T., Otto-bliesner, B.L., Miller, G.H., Daniel, R., Alley, R.B., Kiehl, J.T., Overpeck, J.T., Otto-bliesner, B.L., Miller, G.H., Muhs, D.R., Alley, R.B., Kiehl, J.T., 2006. Paleoclimatic evidence for future ice-sheet instability and rapid sea-level rise. *Science*, *311*(5768), 1747-1750.

Pavesi, M., 2009. Architettura stratigrafica dei depositi medio-e tardoquaternari del bacino padano, finalizzata alla caratterizzazione geometrica degli acquiferi.

Peeters, J., Busschers, F.S., Stouthamer, E., 2015. Fluvial evolution of the Rhine during the last interglacial-glacial cycle in the southern North Sea basin: A review and look forward. Quat. Int. 357, 176–188. https://doi.org/10.1016/j.quaint.2014.03.024

Peeters, J., Busschers, F.S., Stouthamer, E., Bosch, J.H.A., Van den Berg, M.W., Wallinga, J., Versendaal, A.J., Bunnik, F.P.M., Middelkoop, H., 2016. Sedimentary architecture and chronostratigraphy of a late Quaternary incised-valley fill: A case study of the late Middle and Late Pleistocene Rhine system in the Netherlands. Quat. Sci. Rev. 131, 211–236. https://doi.org/10.1016/j.quascirev.2015.10.015

Peeters, J., Cohen, K.M., Thrana, C., Busschers, F.S., Martinius, A.W., Stouthamer, E., Middelkoop, H., 2019. Preservation of Last Interglacial and Holocene transgressive systems tracts in the Netherlands and its applicability as a North Sea Basin reservoir analogue. Earth-Science Rev. 188, 482–497. https://doi.org/10.1016/j.earscirev.2018.10.010

Picotti, V., Pazzaglia, F.J., 2008. A new active tectonic model for the construction of the Northern Apennines mountain front near Bologna (Italy). J. Geophys. Res. Solid Earth 113, 1–24. https://doi.org/10.1029/2007JB005307

Pieri, M., Groppi, G., 1981. Subsurface geological structure of the Po Plain, Italy. Verlag nicht ermittelbar.

Pirazzoli, P.A., 1993. Global sea-level changes and their measurement. Glob. Planet. Change 8, 135–148. https://doi.org/10.1016/0921-8181(93)90021-F

Pondrelli, S., Salimbeni, S., Perfetti, P., Danecek, P., 2012. Quick regional centroid moment tensor solutions for the Emilia 2012 (northern Italy) seismic sequence. Ann. Geophys. 55, 615–621.

https://doi.org/10.4401/ag-6146

Prescott, J.R., Hutton, J.T., 1994. Cosmic ray contributions to dose rates for luminescence and ESR dating: large depths and long-term time variations. Radiat. Meas. 23, 497–500.

Ramsey, C.B., Lee, S., 2013. Recent and Planned Developments of the Program OxCal. Radiocarbon 55, 720–730. https://doi.org/10.1017/s0033822200057878

Regione Emilia-Romagna and Eni-Agip, 1998. Riserve idriche sotterranee della Regione Emilia-Romagna. Ed. by G. Di Dio, Publ. by Publ. by SELCA, Firenze 120.

Regione Lombardia and Eni Divisione Agip, 2002. Geologia degli acquiferi padani della Regione Lombardia. SELCA, Firenze.

Reimer, P.J., Edouard Bard, B., Alex Bayliss, B., Warren Beck, B.J., Paul Blackwell, B.G., Christopher Bronk Ramsey, B., 2013. Intcal13 and Marine13 Radiocarbon Age Calibration Curves 0–50,000 Years Cal Bp. Radiocarbon 55, 1869–1887. https://doi.org/10.1017/S0033822200048864

Ricci Lucchi, F., Colalongo, M.L., Cremonini, G., Gasperi, G., Iaccarino, S., Papani, G., Raffi, S., Rio, D., 1982. Evoluzione sedimentaria e paleogeografica nel margine appenninico. Guid. alla Geol. del margine appenninico-padano. Soc. Geol. It 17–46.

Richter, D., Richter, A., Dornich, K., 2015. Lexsyg smart—a luminescence detection system for dosimetry, material research and dating application. Geochronometria 42.

Rohling, E.J., Grant, K., Hemleben, C., Siddall, M., Hoogakker, B.A.A., Bolshaw, M., Kucera, M., 2008. High rates of sea-level rise during the last interglacial period. Nat. Geosci. 1, 38–42. https://doi.org/10.1038/ngeo.2007.28

Rossi, M., Minervini, M., Ghielmi, M., Rogledi, S., 2015. Messinian and Pliocene erosional surfaces in the Po Plain-Adriatic Basin: Insights from allostratigraphy and sequence stratigraphy in assessing play concepts related to accommodation and gateway turnarounds in tectonically active margins. Mar. Pet. Geol. 66, 192–216. https://doi.org/10.1016/j.marpetgeo.2014.12.012

Rovere, A., Raymo, M.E., Vacchi, M., Lorscheid, T., Stocchi, P., Gómez-Pujol, L., Harris, D.L., Casella, E., O'Leary, M.J., Hearty, P.J., 2016. The analysis of Last Interglacial (MIS 5e) relative sea-level indicators: Reconstructing sea-level in a warmer world. Earth-Science Rev. 159, 404–427. https://doi.org/10.1016/j.earscirev.2016.06.006

Royden, L., Patacca, E., Scandone, P., 1987. Segmentation and configuration of subducted lithosphere in Italy: an important control on thrust-belt and foredeep-basin evolution. Geology 15, 714–717. https://doi.org/10.1130/0091-7613(1987)15<714:SACOSL>2.0.CO;2

Sánchez Goñi, M.F., Bakker, P., Desprat, S., Carlson, A.E., Van Meerbeeck, C.J., Peyron, O., Naughton, F., Fletcher, W.J., Eynaud, F., Rossignol, L., Renssen, H., 2012. European climate optimum and enhanced Greenland melt during the last interglacial. Geology 40, 627–630. https://doi.org/10.1130/G32908.1

Sánchez Goñi, M.F., Eynaud, F., Turon, J.L., Shackleton, N.J., 1999. High resolution palynological record off the Iberian margin: Direct land-sea correlation for the Last Interglacial complex. Earth Planet. Sci. Lett. 171, 123–137. https://doi.org/10.1016/S0012-821X(99)00141-7

Scarponi, D., Kaufman, D., Amorosi, A., Kowalewski, M., 2013. Sequence stratigraphy and the resolution of the fossil record. Geology 41, 239–242.

Scarponi, D., Kowalewski, M., 2004. Stratigraphic paleoecology: Bathymetric signatures and sequence overprint of mollusk associations from upper Quaternary sequences of the Po Plain, Italy. Geology 32, 989–992. https://doi.org/10.1130/G20808.1

Scrocca, D., Carminati, E., Doglioni, C., Marcantoni, D., 2007. Slab retreat and active shortening along the central-northern Apennines, in: Thrust Belts and Foreland Basins. Springer, pp. 471–487.

Shackleton, N.J., 2000. The 100,000-year ice-age cycle identified and found to lag temperature, carbon dioxide, and orbital eccentricity. Science 289, 1897–1902. https://doi.org/10.1126/science.289.5486.1897

Shackleton, N.J., 1987. Oxygen isotopes, ice volume and sea level. Quat. Sci. Rev. 6, 183–190.

Shackleton, N.J., 1969. The last interglacial in the marine and terrestrial records. Proc. R. Soc. London. Ser. B. Biol. Sci. 174, 135–154.

Shackleton, N.J., Sánchez-Goñi, M.F., Pailler, D., Lancelot, Y., 2003. Marine isotope substage 5e and the Eemian interglacial. Glob. Planet. Change 36, 151–155. https://doi.org/10.1016/S0921-8181(02)00181-9

Siddall, M., Rohling, E.J., Almogi-Labin, A., Hemleben, C., Meischner, D., Schmelzer, I., Smeed, D.A., 2003. Supplementary Information: Sea-level fluctuations during the last glacial cycle. Nature 423, 0–5. https://doi.org/10.1038/nature01687.1.

Stammer, D., Wal, R.S.W., Nicholls, R.J., Church, J.A., Le Cozannet, G., Lowe, J.A., Horton, B.P., White, K., Behar, D., Hinkel, J., 2019. Framework for High-End Estimates of Sea Level Rise for Stakeholder Applications, Earth’s Future. https://doi.org/10.1029/2019ef001163

Tanabe, S., Nakanishi, T., Matsushima, H., Hong, W., 2013. Sediment accumulation patterns in a tectonically subsiding incised valley: Insight from the Echigo Plain, central Japan. Mar. Geol. 336, 33–43. https://doi.org/10.1016/j.margeo.2012.11.006

Tanabe, S., Saito, Y., Lan Vu, Q., Hanebuth, T.J.J., Lan Ngo, Q., Kitamura, A., 2006. Holocene evolution of the Song Hong (Red River) delta system, northern Vietnam. Sediment. Geol. 187, 29–61. https://doi.org/10.1016/j.sedgeo.2005.12.004

Tanabe, S., Tateishi, M., Shibata, Y., 2009. The sea-level record of the last deglacial in the Shinano River incised-valley fill, Echigo Plain, central Japan. Mar. Geol. 266, 223–231. https://doi.org/10.1016/j.margeo.2009.08.011

Törnqvist, T.E., Wallinga, J., Murray, A.S., De Wolf, H., Cleveringa, P., De Gans, W., 2000. Response of the Rhine-Meuse system (west-central Netherlands) to the last Quaternary glacio-eustatic cycles: A first assessment. Glob. Planet. Change 27, 89–111. https://doi.org/10.1016/S0921-8181(01)00072-8

Toscani, G., Bonini, L., Ahmad, M.I., Bucci, D. Di, Giulio, A. Di, Seno, S., Galuppo, C., 2014. Opposite verging chains sharing the same foreland: Kinematics and interactions through analogue models (Central Po Plain, Italy). Tectonophysics 633, 268–282. https://doi.org/10.1016/j.tecto.2014.07.019

Tropeano, M., Cilumbriello, A., Sabato, L., Gallicchio, S., Grippa, A., Longhitano, S.G., Bianca, M., Gallipoli, M.R., Mucciarelli, M., Spilotro, G., 2013. Surface and subsurface of the Metaponto Coastal Plain (Gulf of Taranto-southern Italy): Present-day- vs LGM-landscape. Geomorphology 203, 115–131. https://doi.org/10.1016/j.geomorph.2013.07.017

Tzedakis, C., 2013. Pollen Records, Last Interglacial of Europe, 2nd ed, Encyclopedia of Quaternary Science: Second Edition. Elsevier B.V. https://doi.org/10.1016/B978-0-444-53643-3.00183-7

Tzedakis, P.C., Drysdale, R.N., Margari, V., Skinner, L.C., Menviel, L., Rhodes, R.H., Taschetto, A.S., Hodell, D.A., Crowhurst, S.J., Hellstrom, J.C., Fallick, A.E., Grimalt, J.O., McManus, J.F., Martrat, B., Mokeddem, Z., Parrenin, F., Regattieri, E., Roe, K., Zanchetta, G., 2018. Enhanced climate instability in the North Atlantic and southern Europe during the Last Interglacial. Nat. Commun. 9.

https://doi.org/10.1038/s41467-018-06683-3
Vis, G.J., Kasse, C., Vandenberghe, J., 2008. Late Pleistocene and Holocene palaeogeography of the Lower Tagus Valley (Portugal): effects of relative sea level, valley morphology and sediment supply. Quat. Sci. Rev. 27, 1682–1709. https://doi.org/10.1016/j.quascirev.2008.07.003
Waelbroeck, C., Labeyrie, L., Michel, E., Duplessy, J.C., McManus, J.F., Lambeck, K., Balbon, E., Labracherie, M., 2002. Sea-level and deep water temperature changes derived from benthic foraminifera isotopic records. Quat. Sci. Rev. 21, 295–305.
Wintle, A.G., Murray, A.S., 2006. A review of quartz optically stimulated luminescence characteristics and their relevance in single-aliquot regeneration dating protocols. Radiat. Meas. 41, 369–391.